Tectonophysics 576–577 (2012) 20–45

Contents lists available at SciVerse ScienceDirect

Tectonophysics

journal homepage: www.elsevier.com/locate/tecto

Structural and microstructural evolution of the Rattlesnake Mountain Anticline (Wyoming, USA): New insights into the Sevier and Laramide orogenic stress build-up in the Bighorn Basin

Nicolas Beaudoin [a,b,*], Rémi Leprêtre [a,b,c], Nicolas Bellahsen [a,b], Olivier Lacombe [a,b], Khalid Amrouch [a,b,c], Jean-Paul Callot [d], Laurent Emmanuel [a,b], Jean-Marc Daniel [c]

[a] UPMC Univ Paris 06, UMR 7193, ISTEP, F-75005, Paris, France
[b] CNRS, UMR 7193, ISTEP, F-75005, Paris, France
[c] Geology Geochemistry Geophysics Direction, IFP Energies Nouvelles, Rueil-Malmaison, France
[d] UMR CNRS TOTAL 5150 "Laboratoire des Fluides Complexes et leurs Réservoirs", Université de Pau et des Pays de l'Adour, I.P.R.A. Avenue de l'Université BP 1155, 64013 PAU Cedex, France

ARTICLE INFO

Article history:
Received 5 November 2011
Received in revised form 26 March 2012
Accepted 28 March 2012
Available online 5 April 2012

Keywords:
Fracture pattern in foreland basins
Stress propagation in the upper crust
Kinematic evolution of basement-cored anticline
Thick-skinned deformation
Bighorn Basin
Rattlesnake Mountain Anticline

ABSTRACT

The Rocky Mountains in western US provide among the best examples of thick-skinned tectonics: following a period of thin-skinned tectonics related to the Sevier orogeny, the compressional reactivation of basement faults gave birth to the so-called Laramide uplifts/arches. The Bighorn basin, located in Wyoming, is therefore a key place to study the transition from thin- to thick-skinned tectonics in orogenic forelands, especially in terms of microstructural and stress/strain evolution. Our study focuses on a classic Laramide structure: the Rattlesnake Mountain Anticline (RMA, Wyoming, USA), a basement-cored anticline located in the western part of the Bighorn basin. Stress and strain evolution analysis in folded sedimentary layers and underlying faulted basement rocks were performed on the basis of combined analyses of fractures, fault-slip data and calcite twinning paleopiezometry. Most of the fractures are related to three main tectonic events: the Sevier thin-skinned contraction, the Laramide thick-skinned contraction, and the Basin and Range extension. Serial balanced cross-sections of RMA and displacement profiles suggest that all thrust faults were coeval, evidencing strain distribution in the basement during faulting. The comparison of RMA with another structure located in the eastern edge of the Bighorn basin, *i.e.* the Sheep Mountain Anticline (SMA), allows to propose a conceptual model for the geometric and kinematic evolution of Laramide-related basement-cored anticlines. Finally, the stress evolution is reconstructed at both the fold scale and the basin scale. We show that the evolution of stress trends and magnitudes was quite similar in both structures (RMA and SMA) during Laramide times (thick-skinned tectonics), in spite of different stress regimes. During Sevier (thin-skinned tectonics) and post-Laramide times, stress trends and fracture patterns were different in these two structures. These results suggest that the distance to the orogenic front influenced the fracture patterns but not the foreland stress magnitudes, which were likely controlled by the structural style.

1. Introduction and aims of the study

The reconstitution of the past kinematic and tectonic history in ancient fold and thrust belts requires constraints on the evolution through space and time of both stress and strain which affected sedimentary cover and basement rocks. The evolution of strain can be characterized at different scales: from the scale of the foreland basin, to the fold/fault scale, down to the scale of microtectonic features. The dynamics of syn-orogenic sedimentation yields information on the crustal- to lithospheric-scale deformation such as formation of foreland flexural basins (e.g. in DeCelles, 1994, 2004; DeCelles et al., 1998; Lin and Watts, 2002; McQuarrie and DeCelles, 2001). At the upper crustal scale, the evolution through time of faults and folds as well as the structural style are key observations to determine both the shortening kinematics and the rheology of crustal rocks. Growth strata analysis (e.g. in Ford et al., 1997; Jordan, 1981), sequential restoration (e.g. Mouthereau et al., 2007), as well as fracture patterns may help to determine shortening kinematics. In particular, a link between the final fold shape and microstructures (fractures and stylolites) has been highlighted (Engelder, 1987; Erslev and Mayborn, 1997; Fischer et al., 1992; McQuillan, 1974; Srivastava and Engelder, 1990; Stearns and Friedman, 1972; Thorbjornsen and Dunne, 1997). However, it has also been shown that fracture analysis can additionally provide insights into the evolution of the fold shape (Amrouch et al., 2010a; Anastasio et al., 1997; Bellahsen et al., 2006a,

* Corresponding author at: UPMC Univ Paris 06, UMR 7193, ISTEP, F-75005, Paris, France.
E-mail address: nicolas.beaudoin@upmc.fr (N. Beaudoin).

0040-1951/$ – see front matter © 2012 Elsevier B.V. All rights reserved.
doi:10.1016/j.tecto.2012.03.036

2006b; Couzens and Dunne, 1994; Roger et al., 2004; Sanderson, 1982; Storti and Salvani, 2001; Tavani et al., 2006).

Nonetheless, recent studies on fold-fracture relationships highlighted that many fracture sets in folded structures are unrelated to fold growth, but instead are linked to earlier or later stress evolution (e.g., Ahmadhadi et al., 2008; Bellahsen et al., 2006a, 2006b; Bergbauer and Pollard, 2004; Guiton et al., 2003; Lacombe et al., 2011; Tavani et al., 2011). Thus, fracture patterns may provide insights not only into the strain history at small-scale but also into the stress evolution before, during, and after folding. Pre-folding fractures may then be the record of stress build-up both at the foreland scale and at the fold scale. To this purpose, fracture analysis can be usefully coupled to studies of paleostress orientations and magnitudes, based on fault-slip data (e.g. Angelier, 1984; 1989) and calcite twinning paleopiezometry, which ensures more robust results (e.g., Amrouch et al., 2010a, 2011; Craddock and Van der Pluijm, 1999; Lacombe et al., 1993, 2007). At the scale of the foreland basin, far-field paleostresses (e.g., collisional stresses transmitted away from the plate boundaries, foreland flexural stresses) can be deciphered through the analysis of pre-folding fractures (Lacombe et al., 2011; Quintà and Tavani, 2012-this issue), while local stress evolution during fold growth can be reconstructed thanks to fold-related fractures (Bellahsen et al., 2006a; Bergbauer and Pollard, 2004; Cooke, 1997; Fischer and Wilkerson, 2000; Savage et al., 2010).

In this contribution, we report the results of new structural and microstructural analyses to constrain the stress and strain evolution of the Laramide Bighorn foreland basin (Wyoming, USA). This work focuses on the Rattlesnake Mountain Anticline (RMA), a famous Laramide folded structure in the western part of the Bighorn basin (Erslev and Rogers, 1993; Neely and Erslev, 2009). RMA is commonly interpreted as a draped basement-cored fold (Stearns, 1978) and was used in numerous studies as a model for other basement-cored folds in thick-skinned orogens (Stone, 1993). This anticline is a major basement uplift of the basin, and its well-exposed structure allows the study of fracture patterns in both the sedimentary cover and the underlying gneissic basement. We first present a new set of serial balanced cross-sections across the Rattlesnake Mountain structure, as well as fault displacement profiles in order to constrain the timing of activation/propagation of the basement thrusts. Second, in order to capture the mechanisms and timing of acquisition of internal strain of folded strata now observed in Laramide fold limbs, we take advantage of the outstanding quality of the outcrops to carry out an analysis of fracture sets with emphasis on both fold-related populations and fracture sets unrelated to folding, and constrain their sequence of development. We finally compare both the fracture sets and the overall structure in Rattlesnake Mountain Anticline with the results of previous structural and microstructural studies of Sheep Mountain Anticline (Amrouch et al., 2010a, 2010b, 2011; Banerjee and Mitra, 2004; Barbier et al., 2012a; Beaudoin et al., 2011; Bellahsen et al., 2006a, 2006b; Fiore Allwardt et al., 2007; Lovely et al., 2010; Savage et al., 2010; Shackelton and Cooke, 2007) in the eastern part of the Bighorn basin, in order to propose a unified kinematic model for Laramide-related basement-cored folding. Finally, using complementary fault-slip data and calcite twin data as indicators of paleostress orientations and magnitudes, we constrain the successive paleostress/strain patterns related to the pre-Laramide, Laramide and post-Laramide regional tectonic history and the mechanisms controlling development of fracture populations at the scale of the Bighorn foreland basin.

2. Geological setting

The NW–SE striking Rattlesnake Mountain Anticline (RMA) is located in the western part of the Bighorn basin (Northwestern Wyoming, USA), in the Sevier-Laramide foreland (Fig. 1). Since the Early Jurassic, a foreland basin formed and, during the Late Cretaceous, the Sevier shortening event caused the development of a thin-skinned fold-and-thrust belt west of the Bighorn basin (Bird, 1998; DeCelles, 2004). Since the end of the Cretaceous, the Bighorn basin has been progressively isolated by basement uplifts (Laramide arches) (DeCelles, 2004). These major structures may be related to the reactivation of inherited basement faults during the Laramide contractional event (Fig. 1c) as proposed by Marshak et al. (2000) for the whole Laramide uplifts.

The Precambrian basement rocks are involved in nearly all the structures of the Bighorn basin (e.g. Blackstone, 1986). Above the basement, folds affected the 7 km-thick sedimentary cover (Fig. 2) (DeCelles et al., 1991; Neely and Erslev, 2009; Pierce, 1966; Pierce and Nelson, 1968). At RMA, the sedimentary cover is composed of Cambrian sandstones of the Flathead and the Gallatin formations separated by the Gros Ventre shaly formation. Those formations are overlain by the Ordovician dolostones of the Bighorn Formation, the Devonian sandstones of the Three Forks formation, the Mississipian limestones/dolostones of the Madison Formation, the Mississipian shales and sandstones of the Amsden Formation, the Pennsylvanian sandstones of the Tensleep Formations, and the Permian limestones of the Phosphoria Formation (Fig. 2, Durdella, 2001).

RMA is a 27 km long and 12 km wide anticline trending NW–SE (Fig. 3); it is the biggest and among the most studied anticline of the Bighorn basin (Brown, 1988, 1993; Erslev, 1986, 1995; Narr and Suppe, 1994; Neely and Erslev, 2009; Stearns, 1978). Its backlimb is gently dipping 15°NE, while the forelimb is dipping 50°SW. The southern end of the fold comprises a non-cylindrical anticline termination (Cedar Mountain), with an oblique E–W striking hinge.

The fold is controlled by a major basement thrust which brings Precambrian gneissic basement rocks onto Cambrian and Ordovician formations (Fig. 3), as shown by the great exposure through the Shoshone Canyon south of the structure (Fig. 4). RMA has been structurally defined as a “draped fold” by Stearns (1978), and Erslev (1995) showed that the basement accommodated the Laramide contractional event with only little penetrative folding of the basement rocks. Rotation and translation of rigid blocks of the basement rocks have been proposed to explain the draped shape of the sedimentary cover (Fig. 4) (Erslev, 1991, 1995; Neely and Erslev, 2009; Stearns, 1978).

In the eastern part of the basin, the Sheep Mountain Anticline (SMA hereinafter) is another famous structure of the Laramide foreland (Fig. 1b). SMA is a 20 km long and 5 km wide asymmetrical fold striking NW–SE. The backlimb dips 30° toward the SW and the forelimb dips 70° toward the NE. The exposed sedimentary cover comprises the Mississipian limestones/dolostones of the Madison Formation, the Mississipian shales and sandstones of the Amsden Formation, the Pennsylvanian sandstones of the Tensleep Formation, and the Permian limestones of the Phosphoria Formation. SMA is classically interpreted as a basement-cored fold related to a SW dipping backthrust soled on the SW-verging Rio thrust (Stanton and Erslev, 2004). Bellahsen et al. (2006a) and Amrouch et al. (2010a) defined several fracture and fault sets on the basis of mechanical/kinematical consistency and accurate relative chronology observations: the earliest set corresponds to pre-folding joints oriented 110°E (“set I”), tentatively related to the Sevier contractional event and later sheared during the Laramide compression. Another set of joints oriented 045°E (“set II”) is mainly related to the Layer Parallel Shortening (LPS) phase of the Laramide contractional event. The fracture population also includes a reverse fault set associated with the Laramide contractional event with a compressional trend of the maximal principal stress (σ_1) oriented 045°E, a set of syn-folding joints oriented 135°E (“set III”) and a late-folding compressional/strike-slip fault set witnessing a Laramide late stage fold tightening that postdates a major part of the exhumation/erosion of the fold (Amrouch et al., 2011). A minor pre-folding set of joints oriented N–S (“set N–S”) was added to this fracture sequence (Amrouch et al., 2010a).

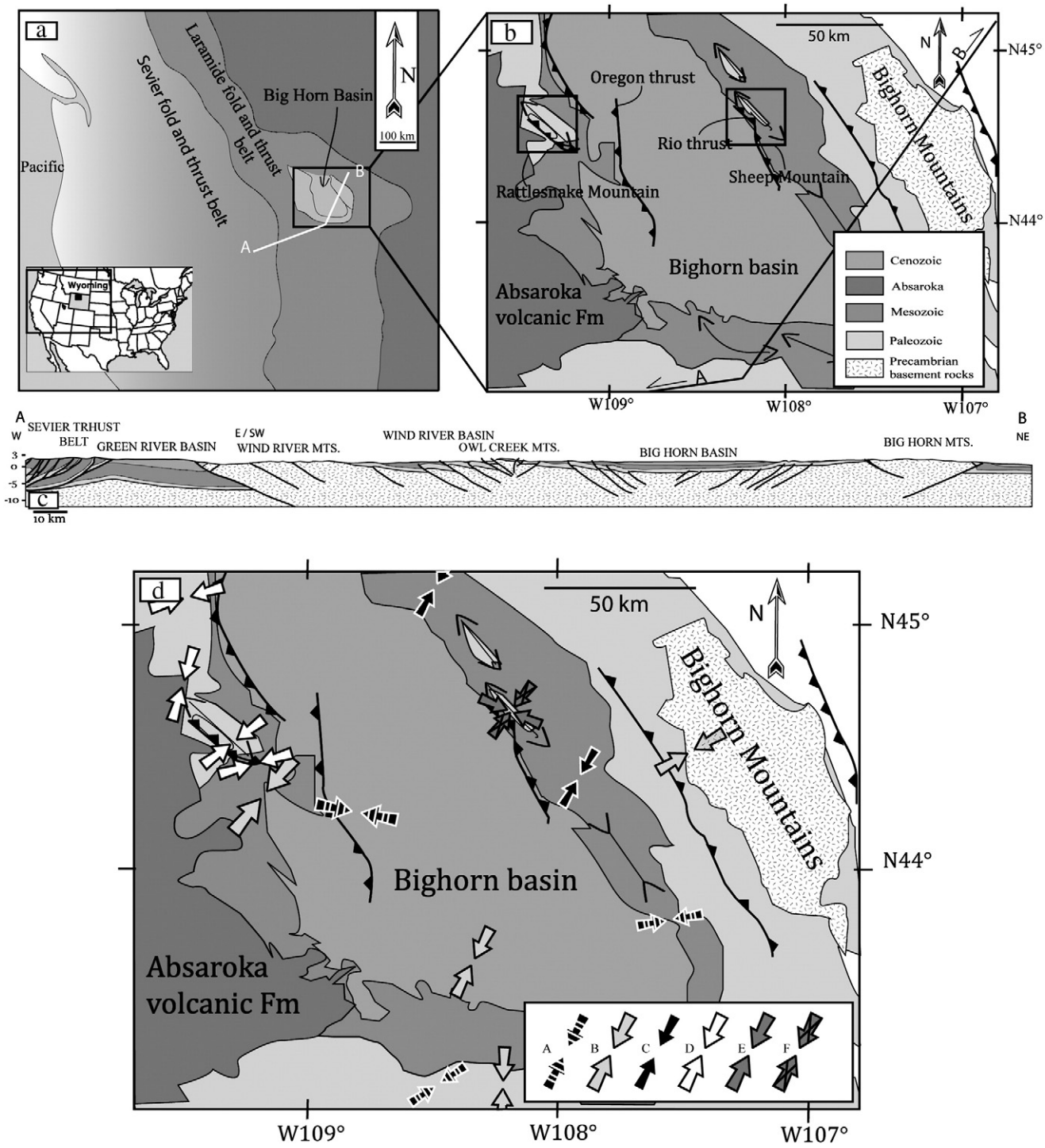

Fig. 1. a- General map of the Bighorn basin (Wyoming, USA), showing the Sevier and Laramide orogenic provinces, along with their respective present-day morphologic fronts. Cross-section is reported as A–B. b – Simplified geological map of the Bighorn basin, with location of Rattlesnake Mountain and Sheep Mountain anticlines, along with major basement faults of the basin. c – W–NE cross section across part of the Sevier belt and the Laramide belt, including the Bighorn basin and the Bighorn Mountains. d- Simplified geological map of the Bighorn basin, with convergent arrows indicating Laramide and Sevier contractional trends reconstructed in previous studies: A. Sevier compressional trends from Craddock and Van der Pluijm (1999); B. Laramide compressional trends from Craddock and Van der Pluijm (1999); C. Laramide compressional trends from Varga (1993); D. Laramide compressional trends from Neely and Erslev (2009); E. Sevier compressional trends from Amrouch et al. (2010a); F. Laramide compressional trends from Amrouch et al. (2010a).

Recent studies further demonstrate differences in the mechanical behaviour of some sedimentary units between SMA and RMA (Barbier et al., 2012a, 2012b–this volume). These differences are mainly due to lithological variations primarily related to contrasting depositional paleoenvironments during the Paleozoic (Pranter et al., 2006). These differences affected the expression of fracture pattern at strata scale, fracture sets being mainly stratabound at SMA except the syn-folding set ("set III"), while most of fracture sets imprinted at RMA are marked instead by vertically connected fractures cutting through the entire stratigraphic column (Barbier et al., 2012a, 2012b–this volume).

Both the kinematic evolution and the sequence of fracture development at RMA will be compared to those available in SMA in order to (1) build a conceptual model of folding and fracture development for Laramide basement-cored folds and (2) to capture

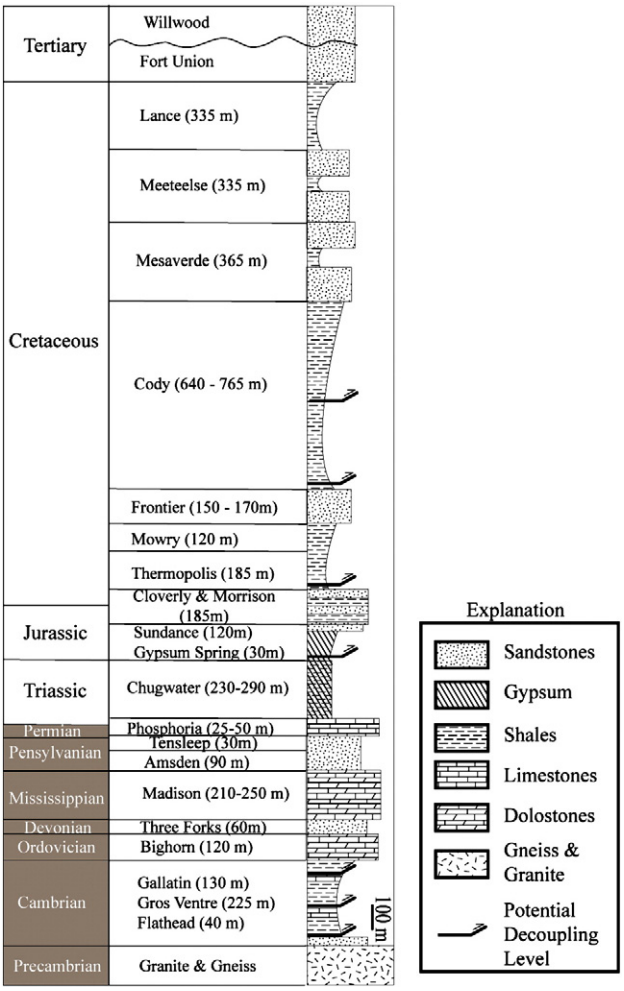

Fig. 2. Synthetic stratigraphic column of the West of the Bighorn basin, modified after Durdella (2001) and Neely and Erslev (2009); mechanical stratigraphy is reported along, with arrows indicating potential decoupling levels. The ages of the formations cropping out at RMA are shown in brown.

the main parameters controlling fracture populations at the scale of the Bighorn basin.

3. Methods for structural and microstructural analyses

3.1. Construction of serial balanced cross sections

Six NE–SW to N–S serial balanced sections were constructed across RMA using available surface geology (Pierce, 1966; Pierce and Nelson, 1968), published subsurface seismic interpretations (Erslev, 1995), and new field observations (Fig. 4). Each cross-section was balanced by considering and restoring the length of the top of the rigid basement, which is mostly brittely deformed (Erslev, 1995; Neely and Erslev, 2009). Both lengths and thicknesses were kept constant for the limestone formations far away from the faults, an assumption consistent with field observations. In contrast, only surfaces of shaly formations were kept constant for balancing, allowing thickness changes as indicated by direct field observations. The balancing of the cross-sections, especially for the overturned strata in the footwall of the fault, is based on the basement wedge concept (Erslev, 1986).

3.2. Fracture analysis

Nearly 3000 fracture orientation data were collected in the most accessible and exposed parts of the fold, including the Cedar Mountain (CM) termination, in both the sedimentary cover and the basement (Table 1). Most of the measurement sites are distributed along two cross-sections (Fig. 3). Only few measurement sites are located near the hinge of RMA, due the scarcity of good quality outcrops in this part of the structure. Fracture populations (or sets) were defined on the basis of common orientation (strike and dip) and mode of deformation (opening or shearing) defined in the field and in thin-sections (cut perpendicular to mineralized vein strike). The mean orientation for each set was computed using a software developed at IFPEN for the automatic definition of fracture clusters (see Bellahsen et al., 2006a).

The results of the analysis are presented on stereonets of the orientation data at each measurement site that are not weighted by abundance, as we believe that this can be biased by outcrop conditions. However, we carefully observed the fracture set characteristics, i.e. systematic pattern (less planar, parallel, and horizontally and vertically through-going), and relative abundance.

Fractures with ambiguous deformation mode will be called simply fractures hereinafter, while fractures clearly opened in mode I will be referred to as joints when empty and as veins when mineralized. Mode I opening is supported either by the lack of positive evidence of shearing and grain crushing along vein boundaries, or by direct observations, such as offsets of preexisting features from the matrix or pressure-solution seams (stylolites) (Fig. 5a,b,d) or by the pattern of crystal growth within the veins (i.e., elongated calcite crystals/fibers growing perpendicular to host–rock/vein interface, bridge-like structures, Fig. 5a,c,d). Joints and veins have been treated the same in the statistical analysis of fracture orientations in accordance with their common opening mode (Engelder, 1987). Joints and veins were considered as indicative of paleostress orientations, paleo-σ_3 axis being perpendicular to their trend. Complementary observations of tectonic stylolites, striated microfaults or calcite twins help additionally constrain the attitude of the paleo-σ_1 axis.

3.3. Fault-slip analysis

Striated faults have been used for a long time to reconstruct paleostress orientations and regimes by means of inversion techniques (e.g., Angelier, 1984). The basic principle consists of finding the best fit between the observed lineations and directions of slip on numerous faults and the theoretical shear stress induced on these planes by the tensor solution of the inverse problem. The results are the local orientation (trend and plunge) of the three principal stress axes σ_1, σ_2 and σ_3 (with $\sigma_1 \geq \sigma_2 \geq \sigma_3$, compression considered positive) and the Φ ratio between differential stress magnitudes ($\Phi = (\sigma_2 - \sigma_3)/(\sigma_1 - \sigma_3)$, with $0 \leq \Phi \leq 1$). This ratio characterizes the shape of the stress ellipsoid, and therefore the actual nature of the stress regime. The quality of the tensor calculated is given by numerical estimators such as the average angle between the computed shear stresses and the actual striations.

3.4. Paleostress reconstruction from calcite twin analysis

Mechanical e-twinning readily occurs in calcite deformed at low temperature. Calcite twinning requires a low critical resolved shear stress of 10 ± 4 MPa, which depends on grain size (e.g., Rowe and Rutter, 1990) and internal twinning strain (Lacombe, 2001; Laurent et al., 2000), and has only a small sensitivity to temperature, strain rate and confining pressure. In order to reconstruct paleostresses recorded by twinned calcite either from host rocks or vein fillings, we used the Etchecopar's method for inverting calcite twin data (Etchecopar, 1984; see details in Lacombe, 2007), which computes simultaneously stress orientations and related differential stresses. The inversion process takes into account both the twinned and the untwinned planes, the latter being those of the potential e-twin planes which never experienced a resolved shear stress of sufficient magnitude to cause twinning. The inverse problem consists of finding the stress tensor that best fits the distribution of twinned and

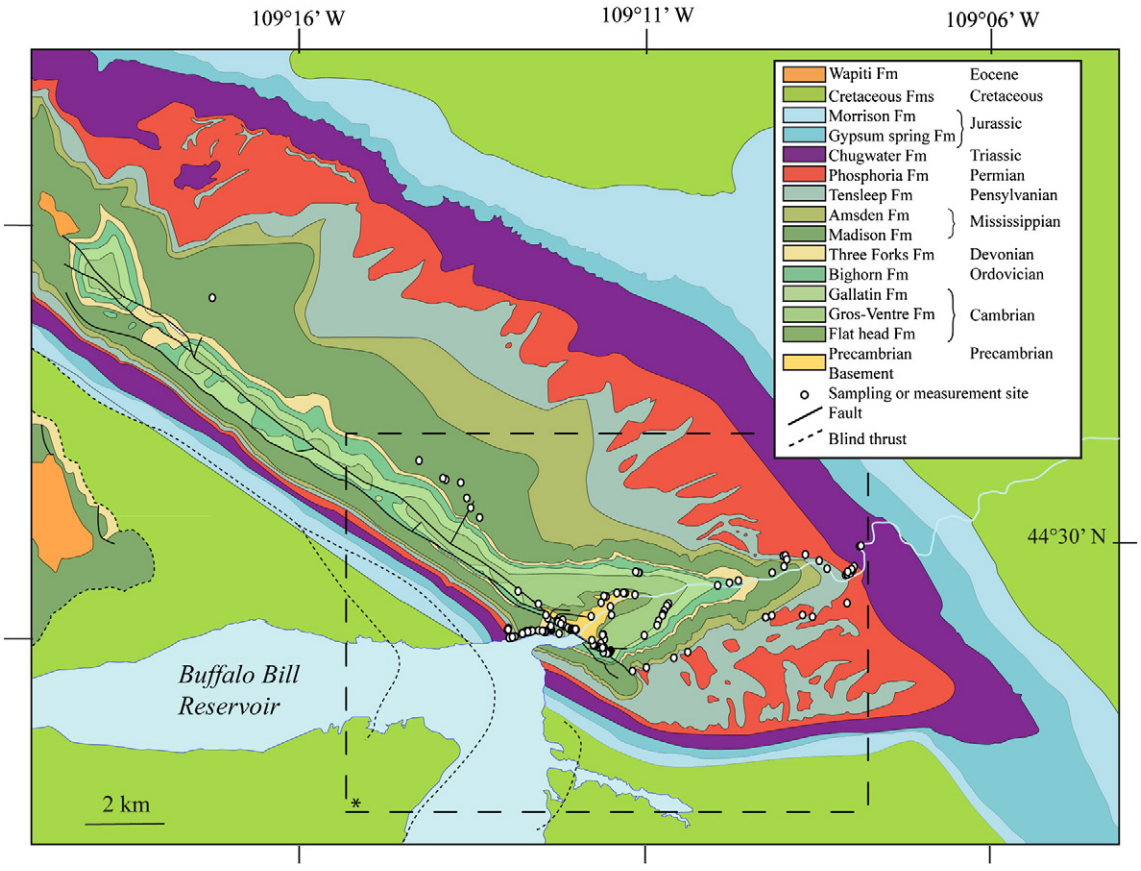

Fig. 3. Simplified geological map of Rattlesnake Mountain Anticline (after Pierce, 1966; Pierce and Nelson, 1968). Dots represent measurement sites and sampling locations. *: Dashed frame represent location of area on Fig. 15.

untwinned planes. The orientations of the three principal stresses σ_1, σ_2, and σ_3 are calculated, together with the Φ ratio [$\Phi = (\sigma_2 - \sigma_3)/(\sigma_1 - \sigma_3)$] (*i.e.*, like for fault slip analysis) and the peak differential stresses ($\sigma_1 - \sigma_3$). If more than ~30% twinned planes in a sample are not explained by a unique stress tensor, the inversion process is repeated with the uncorrelated twinned planes and the whole set of untwinned planes. This process provides an efficient way of separating superimposed twinning events where polyphased deformation has

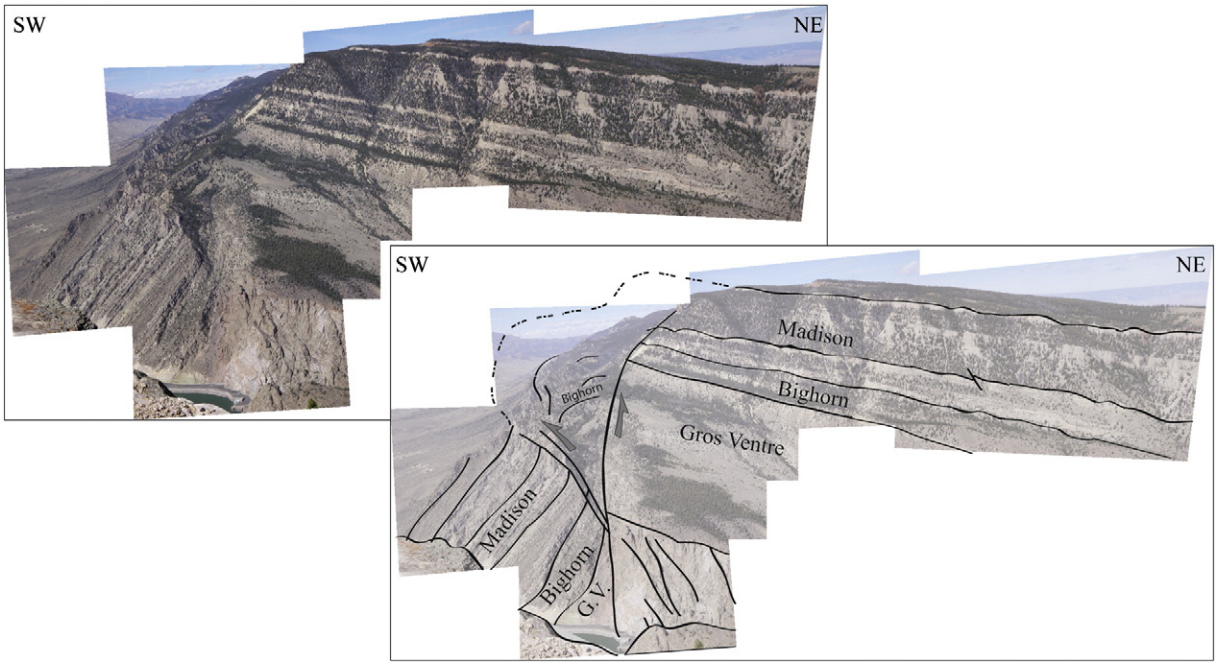

Fig. 4. Photograph and interpretation of Rattlesnake Mountain Anticline viewed from Cedar Mountain, south of Shoshone Canyon. Overturned strata in the forelimb highlight the late propagation of reverse fault splays.

Table 1
Characteristics of sites of fracture measurements.

Site	Latitude	Longitude	Formation
111	44° 30' 0,30" N	109° 12' 0,43" W	Phosphoria
112	44° 30' 0,88" N	109° 11' 58,80" W	Tensleep
114	44° 30' 4,69" N	109° 11' 46,73" W	Madison
117	44° 30' 32,98" N	109° 10' 17,69" W	Basement
118	44° 30' 4,88" N	109° 11' 44,75" W	Madison
119	44° 30' 4,93" N	109° 11' 43,73" W	Madison
121	44° 30' 3,23" N	109° 11' 17,43" W	Bighorn
122	44° 30' 3,48" N	109° 11' 50,04" W	Madison
123	44° 30' 3,06" N	109° 11' 51,43" W	Madison
125	44° 30' 11,60" N	109° 11' 18,39" W	Bighorn
128	44° 30' 13,19" N	109° 11' 14,29" W	Basement
131	44° 30' 6,78" N	109° 11' 26,19" W	Bighorn
132	44° 30' 6,72" N	109° 11' 25,27" W	Bighorn
137	44° 30' 24,92" N	109° 11' 36,18" W	Flathead
138	44° 30' 34,21" N	109° 11' 54,55" W	Gallatin
139	44° 30' 38,34" N	109° 8' 54,34" W	Bighorn
140	44° 30' 15,02" N	109° 8' 10,96" W	Tensleep
142	44° 30' 16,24" N	109° 8' 5,10" W	Tensleep
143	44° 30' 16,60" N	109° 7' 37,68" W	Phosphoria
145	44° 30' 25,45" N	109° 6' 57,30" W	Phosphoria
146	44° 30' 4,60" N	109° 11' 45,99" W	Madison
212	44° 31' 0,83" N	109° 7' 34,84" W	Phosphoria
615	44° 30' 0,10" N	109° 12' 2,52" W	Phosphoria
616	44° 30' 0,73" N	109° 11' 59,73" W	Phosphoria
618	44° 30' 3,47" N	109° 11' 49,60" W	Madison
619	44° 30' 4,60" N	109° 11' 45,99" W	Madison
620	44° 30' 5,27" N	109° 11' 32,37" W	Three Forks
621	44° 30' 5,20" N	109° 11' 32,74" W	Three Forks
629	44° 29' 45,52" N	109° 9' 33,86" W	Tensleep
630	44° 29' 38,27" N	109° 9' 58,45" W	Amsden
632	44° 30' 16,61" N	109° 10' 30,09" W	Flathead
634	44° 29' 50,54" N	109° 10' 30,68" W	Gros Ventre
635	44° 29' 58,88" N	109° 10' 36,66" W	Gros Ventre
637	44° 30' 6,00" N	109° 11' 7,52" W	Basement
638	44° 30' 6,13" N	109° 11' 2,20" W	Basement
642	44° 30' 30,61" N	109° 10' 36,93" W	Basement
643	44° 30' 6,97" N	109° 11' 8,93" W	Basement
644	44° 30' 7,52" N	109° 11' 9,59" W	Basement
645	44° 30' 6,68" N	109° 11' 6,35" W	Basement
650	44° 30' 25,83" N	109° 10' 39,59" W	Flathead
652	44° 34' 8,38" N	109° 16' 31,03" W	Madison
653	44° 32' 9,38" N	109° 13' 24,00" W	Madison
656	44° 31' 27,75" N	109° 12' 29,45" W	Madison
662	44° 29' 49,38" N	109° 10' 31,88" W	Gros Ventre
664	44° 29' 48,60" N	109° 10' 33,26" W	Gros Ventre
675	44° 30' 25,17" N	109° 9' 38,75" W	Gros Ventre
676	44° 30' 23,33" N	109° 9' 40,31" W	Gros Ventre
691	44° 29' 52,71" N	109° 10' 38,93" W	Gros Ventre
701	44° 30' 47,54" N	109° 10' 4,98" W	Gallatin
704	44° 30' 1,90" N	109° 10' 0,38" W	Gallatin
764	44° 30' 41,76" N	109° 8' 35,38" W	Three Forks
767	44° 30' 47,73" N	109° 8' 4,95" W	Bighorn

occurred (Amrouch et al., 2010a; Lacombe et al., 1990, 1993; Rocher et al., 1996).

3.5. Reconstruction of paleostress evolution using Mohr construction

In order to decipher the first-order evolution of principal stress magnitudes during the fold history, we further combined in a Mohr construction the results of calcite twinning paleopiezometry, fracture/micro-fault analysis and rock mechanics data (Amrouch et al., 2011; Lacombe, 2001; Lacombe and Laurent, 1992). For each deformation sub-stage, differential stresses derived from calcite twinning constrain the diameter of the Mohr circles, so the values of the principal stresses σ_1, σ_2 and σ_3 can be determined by fitting the Mohr circles to either the Byerlee's curve to account for frictional sliding along preexisting planes or to the failure envelope for newly formed faulting/fracturing. For the latter, and despite lithological variations between RMA and SMA, we used in this paper the Crack Development Curve (CDC) available for the Madison formation determined by rock mechanics tests on SMA samples (Amrouch et al., 2011).

3.6. From relative chronology of microstructures to chronology of paleostress regimes

The analysis of the attributes of micro/mesostructures (fractures, striated mesofaults, calcite twins) and of their variability across the fold enable to constrain the relative timing between development of these structures and folding. In particular, we distinguish hereinafter pre-tilting, syn-tilting and post-tilting structures. Among pre-tilting structures, the distinction between pre-folding and early-folding fractures is based on the kinematic consistency with folding: while an early-folding fracture set formed during LPS (at still negligible folding or at the onset of folding) in a consistent stress field (*i.e.*, a fold-related extensional cross-axial fracture set or oblique shear fracture set), a pre-folding set also predates bed tilting but has originated in a different earlier stress field (*i.e.*, during a LPS phase unrelated to stress field consistent with folding). Syn-tilting structures formed during fold growth/amplification (*i.e.*, syn-folding *ss*). Post-tilting structures may be late-folding if they formed in a stress field consistent with folding (e.g., late stage fold tightening) or post-folding if they have originated in a late different stress field (unrelated to folding). Early-folding, syn-folding and late-folding fractures therefore developed in the period spanning from (blind thrust propagation and) negligible folding to late stage fold tightening and thus can be classified as syn-folding *sl* (see also Tavani et al., 2006).

3.6.1. Chronology of fractures

As mentioned earlier, members of a fracture set share both a common range of orientations and a common deformation mode. Commonality of fracture orientation after removal of bedding dip, where the fractures are bed-perpendicular, was taken as supportive of a pre-tilting origin (Bellahsen et al., 2006a; Hancock, 1985).

Fractures striking either perpendicular or parallel to bedding strike are not affected by rotation of bedding to remove the dip and may be interpreted as occurring during any stage of fold growth. To unfold the orientation data, we assumed that the sites did not suffer any rotation around a vertical axis and that the local fold axis is horizontal. Under these assumptions, fracture data were unfolded using the rotation necessary to bring the average bedding back to its horizontal attitude. Diagrams of raw and unfolded fracture sets are presented in order to discuss their age relative to folding. This chronology is of primary importance to constrain relationships between fracturing and folding in time and space and to establish a link between this chronology and the regional tectonic evolution. As fractures were sampled in all structural positions within various formations, our data set will help delineate the micro- and meso-scale deformation pattern before and after, and possibly during fold growth. Relative chronology among pre-folding or post-folding fracture sets can be further constrained on the basis of consideration on the regularity of length and spacing of fractures (a fracture set with steady length or spacing in strata can be reliably considered as older than the others), in addition to careful examination of statistical crosscutting/abutting relationships observed both in the field and in thin sections.

3.6.2. Chronology of faults and related stress tensors

The identification and separation of successive generations of faults and related stress regimes is based on both mechanical incompatibility between fault slips (individual misfits of fault slip with the computed stress tensors) and relative chronology observations (superimposed striations on fault surfaces, crosscutting relationships between faults). As for fracture sets analysis, particular attention was paid to horizontal-axis rotations of rock masses due to folding. Assuming that a principal stress axis is vertical (Anderson, 1951), if a fault set measured in a fold limb formed before strata

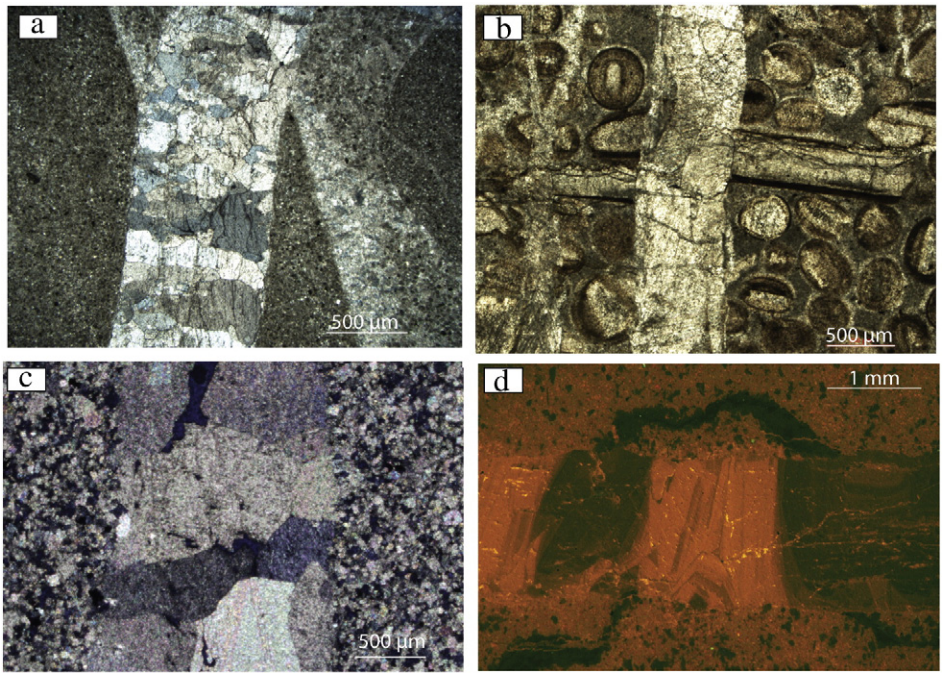

Fig. 5. Photomicrographs of thin sections observed under polarized light (a, b, c) or under cathodoluminescence (d). Mode I opening is supported by the offset of some elements of the matrix (a, b), by the offset of pre-existing stylolites (d) or by the existence of syntaxial growth of calcite crystals (a, c).

tilting and was subsequently tilted, one of the computed stress axes is generally found perpendicular to bedding, whereas the two others lie within the bedding plane. In such a case, the fault system can be interpreted as pre-tilting (pre/early-folding). In contrast, tensors having compression axes that are horizontal irrespective of bedding dip are interpreted as post-tilting (late/post-folding); tensors with compression axes inclined consistently less than, but in the same direction as bedding dip are interpreted as syn-tilting/folding. Note that the pre-tilting nature of fault systems and of related paleostress tensors can be assessed independently of the assumption of an Andersonian stress regime. A pre-tilting fault system is reliably identified if the related fault–slip data collected across the entire fold (hence with various strata attitude), yield after unfolding a more consistent stress solution (in terms of scattering of orientations and numerical quality estimators) than the folded data. In such a case, the assumption is made that a uniform tensor is preferred to a varying tensor, or, that a low misfit solution is preferred to a high misfit solution, in a way similar to the so-called 'fold-test' for paleomagnetic data (see discussion in Lacombe, 2012).

3.6.3. Chronology of twinning events and related stress tensors

The chronology of twinning events and related stress tensors can be constrained first by comparing calcite twinning strain preserved in matrix (which presumably recorded the entire twinning history, at least the earliest stages since calcite may harden once twinned) and in the different vein sets. Furthermore, the relative chronology between successive stress regimes recorded in twinned calcite from a vein filling can be established by considering that a stress tensor with a σ_3 axis perpendicular to the vein strike is likely related to the vein formation, while superimposed tensors with stress axes inconsistent with the vein geometry reflect post-opening stress regimes (e.g., Lacombe, 2010). Finally, like for faults, sampling in fold limbs also constrains the chronology of twinning relative to folding. If a twin set formed during the initial phase of layer-parallel shortening (LPS) and was subsequently tilted with the strata during folding, then one axis of the stress tensor should be perpendicular to bedding and the others would expectedly lie within the bedding plane. In contrast, late or post-folding twin sets should yield two horizontal stress axes and one vertical. For instance, early-folding, LPS-related stress tensors have maximum compression axes inclined consistently and with the same dip as the bedding, while those with maximum compression axes that are horizontal irrespective of bedding dip are either related to late stage fold tightening or post-date folding. Stress tensors with maximum compression axes inclined consistently less than, but in the same direction as bedding dip, may reflect either syn-folding twinning (Lacombe, 2001) or rotation of pre-folding twins at the grain scale due to flexural slip (Harris and Van der Pluijm, 1998).

4. Results

4.1. Balanced cross-sections

The balanced cross-sections of RMA by Erslev (1986) and Neely and Erslev (2009) are based on the basement wedge concept in order to account for the space problem in the footwall highlighted in the previous cross sections (Stearns, 1978). These balanced cross-sections involve rotation of basement blocks above steep basement faults and assume no penetrative deformation in the basement, distributed deformation within the cover, and thickness variations in shale and limestone units (namely the Mississippian Madison Fm.) in the hanging wall and in the vertical forelimb (Neely and Erslev, 2009).

Nevertheless, new field observations in the forelimb suggest the existence of small-scale folds and secondary reverse fault splays (dipping 50° to 60°NE) below the main thrust and no major thickness change in the limestones of the Madison Fm. The forelimb of RMA is overturned, and was cut by NE dipping late reverse faults (Fig. 4). New serial balanced cross-sections have been built through Rattlesnake Mountain and Cedar Mountain anticlines (Fig. 6) to better constrain the kinematic evolution of both structures. These sections show that only two reverse fault splays penetrated into the cover sequence, with their upper tips located within the Madison Fm., consistently with the previous cross-sections of RMA (Erslev, 1995; Neely and Erslev, 2009; Stearns, 1978). Sections also assume partially overturned eroded strata in the forelimb, in agreement with field observations. In our interpretation, the basement wedge is

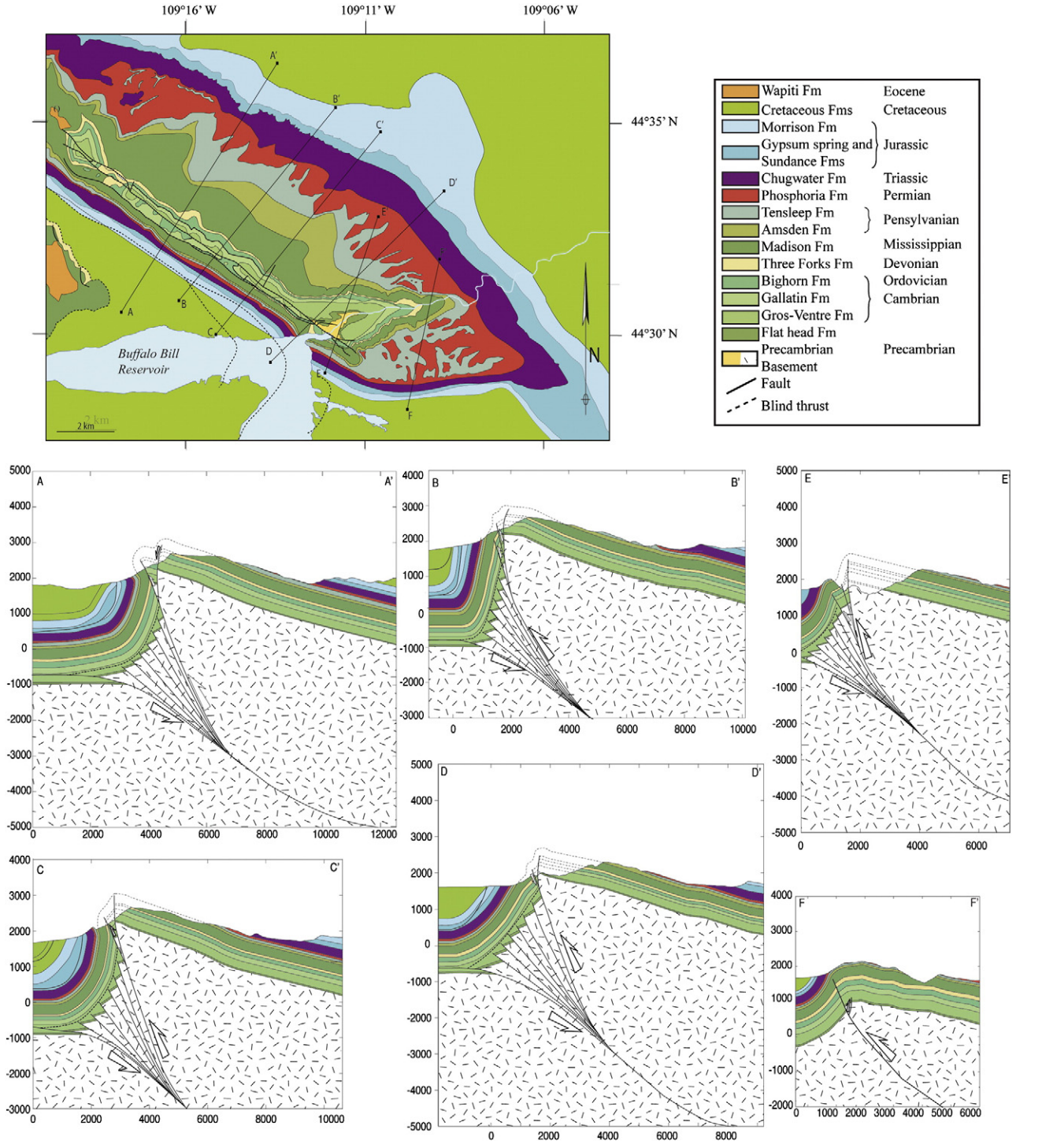

Fig. 6. Serial balanced cross-sections constructed at RMA. Deformation within the so-called basement wedge is shown as numerous fault splays (their number is obviously unconstrained, 6 are represented for the sake of simplicity). The dotted line in the Gros Ventre fm. represents the level of decoupling implied by the basement wedge concept (see text for details). For sedimentary formations, same key as in Fig. 3. Point labeled "O" on the map refers to the northwestern origin used for the displacement profiles presented in Fig. 8.

considered as involving many reverse faults that localize deformation in the basement rocks, limiting by this way the amount of shear distributed in the entire overlying sedimentary cover. A zone of decoupling is proposed in the upper part of the shaly Gros Ventre Fm. to accommodate deformation above the basement rocks by internal deformation (disharmony) without affecting other formations. The amount of basement shortening ranges between 8% (730 m in CM) and 28% (4,5 km) (e.g. Fig. 7); the mean value of 20% (about 2 km, Fig. 8) is consistent with the 1,6 km of shortening deduced from the balanced cross-section proposed by Erslev (1986; 1995).

Assuming that the rotation of the hanging wall basement block was about 12° as predicted by Erslev (1986), the secondary reverse fault splays have the same dip (within a 5° range) than some of the basement fractures (Fig. 4). Nevertheless, as there is no evidence that these fault splays cross-cut the main basement thrust, we interpreted the splays as soling out on the main basement thrust. Moreover, these secondary faults seem to cut across the sub-vertical forelimb, suggesting a late propagation in the sedimentary cover.

A displacement profile along the fault planes has been calculated based on the cross-sections and the offset of the basement top (Fig. 8),

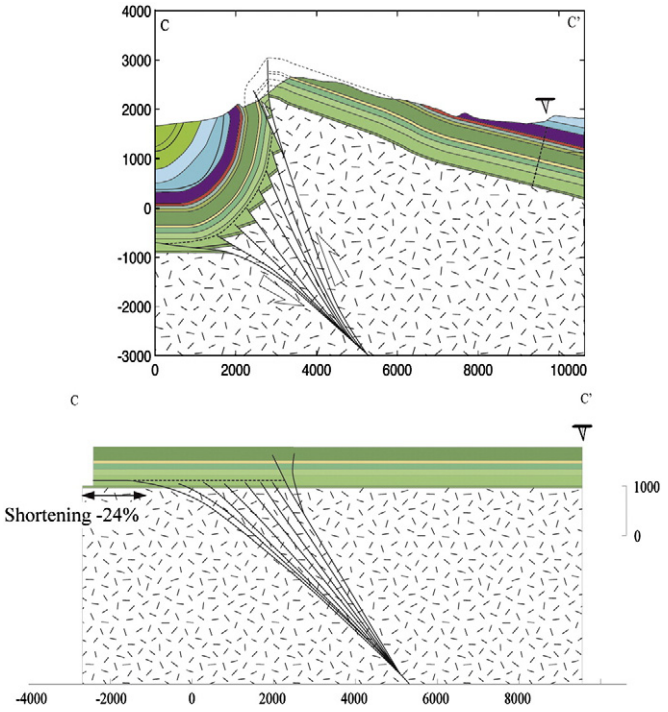

Fig. 7. Example of balanced cross-section restoration on cross-section C–C' (see Fig. 6 for location).

which is the interface wherein the maximum of deformation is accommodated by thrusting if neither penetrative deformation nor folding is considered in the basement (Erslev, 1986, 1995; Neely and Erslev, 2009). Moreover, the depth to the basement is constrained by seismic data at the SW of the fold and in the NE the interface has been mapped in details by GPS data (Erslev, 1995). The displacement profile is reported for the three mapped thrusts (Pierce, 1966; Pierce and Nelson, 1968); a cumulative displacement profile is also shown. Displacement along fault planes appears to be large on the steepest fault in the NW part of RMA while it is small on the main basement

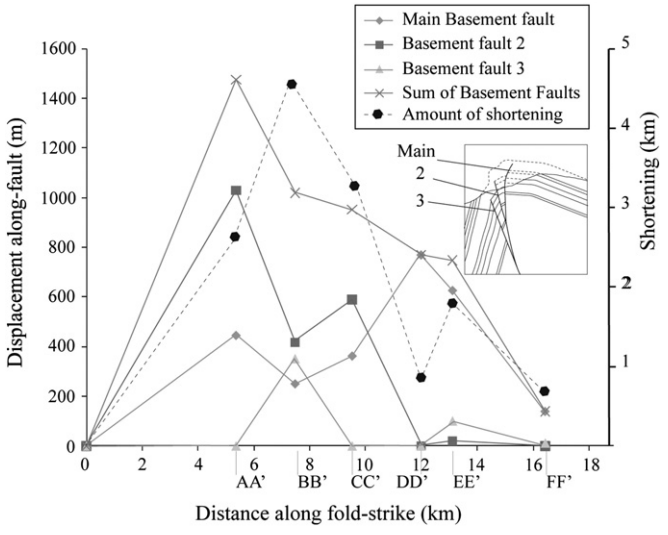

Fig. 8. Displacement-distance profiles reconstructed along the strike of Rattlesnake Mountain for each fault of the superficial fault splays (inset). Light grey diamonds represent the main basement fault, dark grey squares represent the displacement profile related to the most superficial of the fault splays, and the light grey triangles represent the displacement profile related to the deepest of the fault splays. Grey crosses represent the cumulative displacement profile of the three faults of the fault splay. Black dot with the dotted line represent the absolute value of shortening at the basement top, calculated from balanced cross sections showed in Fig. 6.

thrust at the SE, toward Cedar Mountain. In other words, the maximum of displacement D_{max} for each fault is not located at the same place (Fig. 8).

A single D_{max} of about 1500 m can be observed on the cumulative profile, in the northwest part of RMA. As demonstrated by Peacock and Sanderson (1991), this result suggests that the faults were linked in space and time. Indeed, the fault linkage model (Cartwright et al., 1995; Peacock and Sanderson, 1991) predicts that faults propagating toward each others can be identified by the shape of the cumulative displacement profile, which exhibits a link between the displacement profile of each single fault, producing higher D_{max}/L ratios, where L is the length of the lateral extension of the fault plane (e.g. Kim and Sanderson, 2005). This "coherent fault" kinematic model, previously defined for normal faults (e.g. Walsh et al., 2002), has been extended to reverse fault populations by Lamarche et al. (2005). Thus, considering the set of fault splays as a fault population, a diachronic propagation of each segment should lead to displacement profiles looking alike each others with an almost common D_{max}. In the case of RMA fault splays, the shape of cumulative displacement profile suggests a coeval propagation of all faults. Moreover, the cumulative profile has a D_{max}/L (L, length of the fault) of about 10^{-1}, which is consistent with the gradient characteristic of inversion of faults (Kim and Sanderson, 2005).

4.2. Sequence of fracture development

Based on the statistical analysis of fracture orientation as well as of chronological relationships (Fig. 9), the fracture population at RMA has been divided into 7 main sets comprising joints, veins and striated microfaults observed on field (Figs. 10–14). The derived sequence of fracture development relies upon more than 170 observations of chronological relationships at both the meso-scale (e.g. Fig. 9), and at the micro-scale on about 100 thin-sections, wherein the deformation mode of veins (here mainly mode I, opening) was checked (e.g. Fig. 5). Fracture sets were defined in 49 measurement sites (Figs. 10–12) covering every structural position and formations/lithologies. Results are presented at the fold-scale (Fig. 10) and in the Shoshone Canyon (southern part of RMA), focusing on the cover formations (Fig. 11), and on the basement rocks (Fig. 12). We have illustrated for some sites (Fig. 9) the workflow for analysing fracture data: the raw fracture data (fracture planes and poles) are shown, along with their interpretation in terms of statistically defined mean sets; finally, unfolded fracture data are shown. For the sake of simplicity however, in Figs. 10–12 only the two diagrams with raw and unfolded data interpreted in terms of mean sets will be shown.

The oldest set (S-I) comprises bed-perpendicular joints and veins striking E–W to 060°E when unfolded. These fractures were measured in 16 sites over 49 at both RMA and CM, and the main strike is E–W. In the forelimb of the fold, some of the fractures of this set were later reactivated as strike-slip/reverse faults during or after folding (Fig. 14, site 122). This set is poorly developed in the basement rocks at RMA.

A gathering of bed-perpendicular joints and veins striking 160°E to 020°E define a second set (S-II) that clearly abuts on, hence postdates, set S-I (Fig. 9b,c,e), although in some places some ladder pattern may alternatively suggest that a minor part of these S-II fractures may be cross-joints (Fig. 9b). This set was largely observed in 16 sites over 49, and its mean strike is N–S to 020°E, with few sites where the mean strike is 160°E (sites 125, 662 and 664, Fig. 11). Thus, these fractures developed in all parts of the folds and are encountered in all lithologies.

Bed-perpendicular joints and veins oriented 110°E–120°E abut on sets S-I and S-II and define the third set (set S-III, Fig. 9c,e). This is the less represented of the 7 main fracture sets at the fold scale (10 sites over 49), but the fractures are the most regularly oriented. They are better developed in CM and at the hinge of the RMA, and are poorly

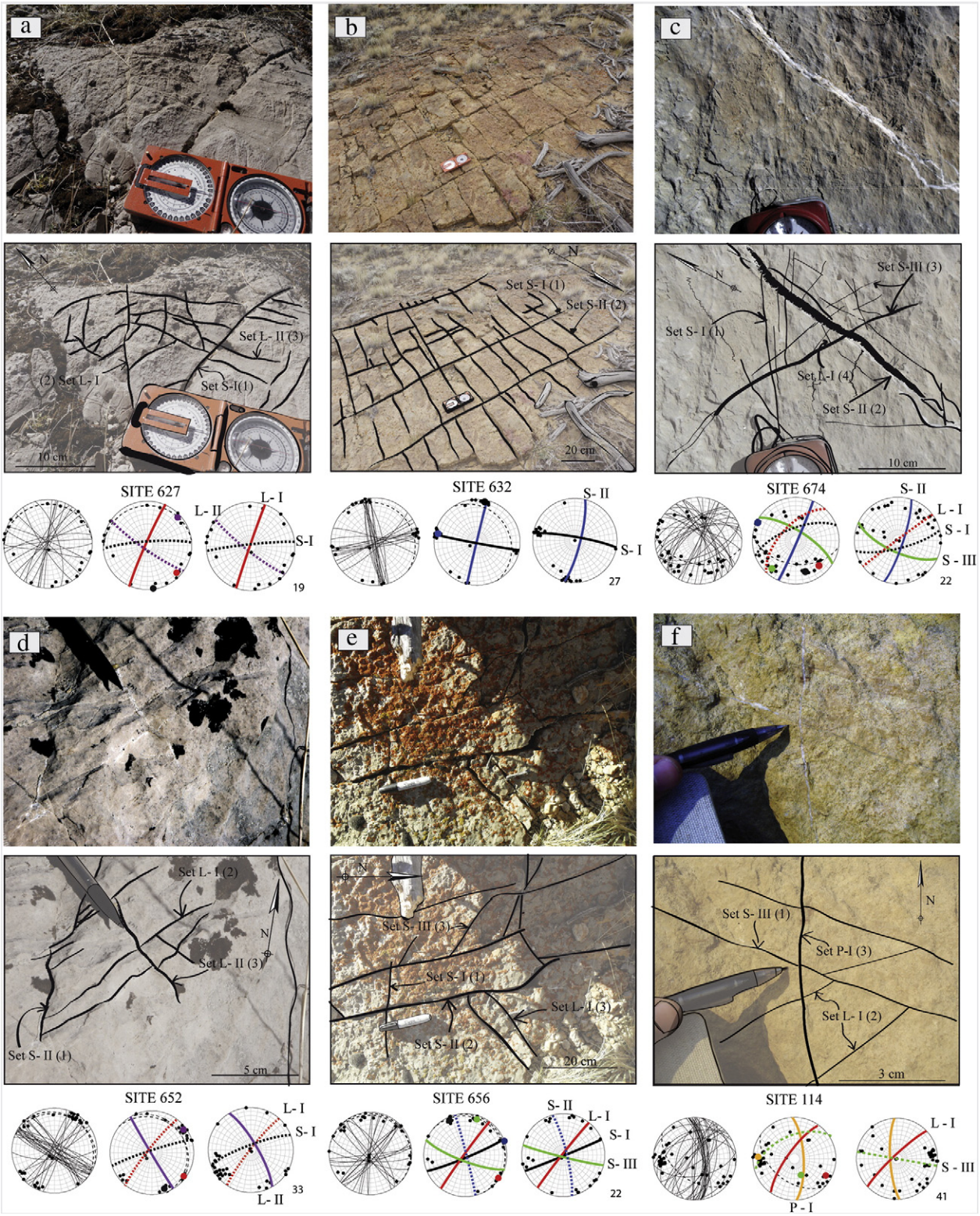

Fig. 9. Photographs and interpretations of some fracture networks along with chronological relationships at Rattlesnake Mountain. Below each photograph are shown stereodiagrams (Schmidt's lower hemisphere) with raw data (fracture planes and poles), statistically computed mean fractures planes and poles defining the fracture sets in the current strata attitude, and the data and mean fracture planes in their unfolded attitude.

represented in the forelimb (Fig. 10, site 618), but they are observed in both cover and basement rocks.

Bed-perpendicular joints/veins oriented about NE–SW (set L-I), perpendicular to the fold axis, abut on sets S-I, S-II, and S-III (Fig. 9a, d–f). This fracture set is the most abundant at the fold scale (24 sites over 49), it strikes from 030°E to 070°E, with a predominant strike of 045°E–050°E, and developed both at RMA and CM in cover rocks, with a mean strike of 050°E. In the basement, their mean strike rotates from 060°E (Fig. 12, sites 117 and 642) to 030°E close to the basement thrust (Fig. 12 sites 637, 638 and 644). In the cover, some strike–slip faults are kinematically consistent with these L-I joints and veins (see Sub-section 4.3 and Figs. 13a, 14).

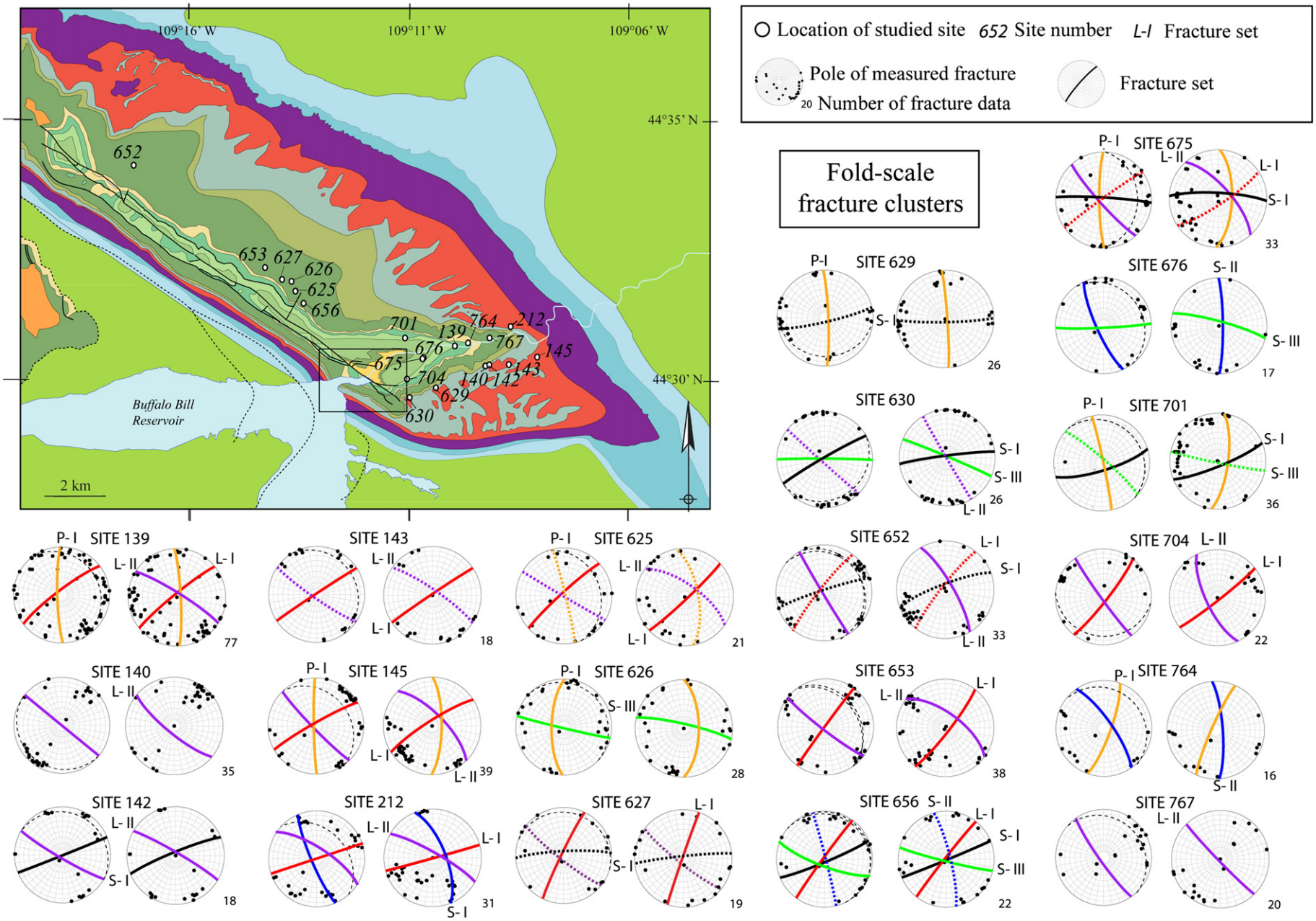

Fig. 10. Results of fracture analysis at the fold-scale, including raw data (poles to fractures) and main fracture set orientations, in their current attitude (left diagram) and in their unfolded attitude (right diagram) (Schmidt's lower hemisphere, equal area stereonets). Black lines represent fractures of set S-I, blue lines of set S-II, green lines of set S-III, red lines represent fractures of set L-I, purple lines of set L-II, and orange lines represent fractures of set P-I. Dashed lines highlight a fracture set which is minor at the scale of the site, but well represented at the fold scale. Same key as in Fig. 3 for the geological map.

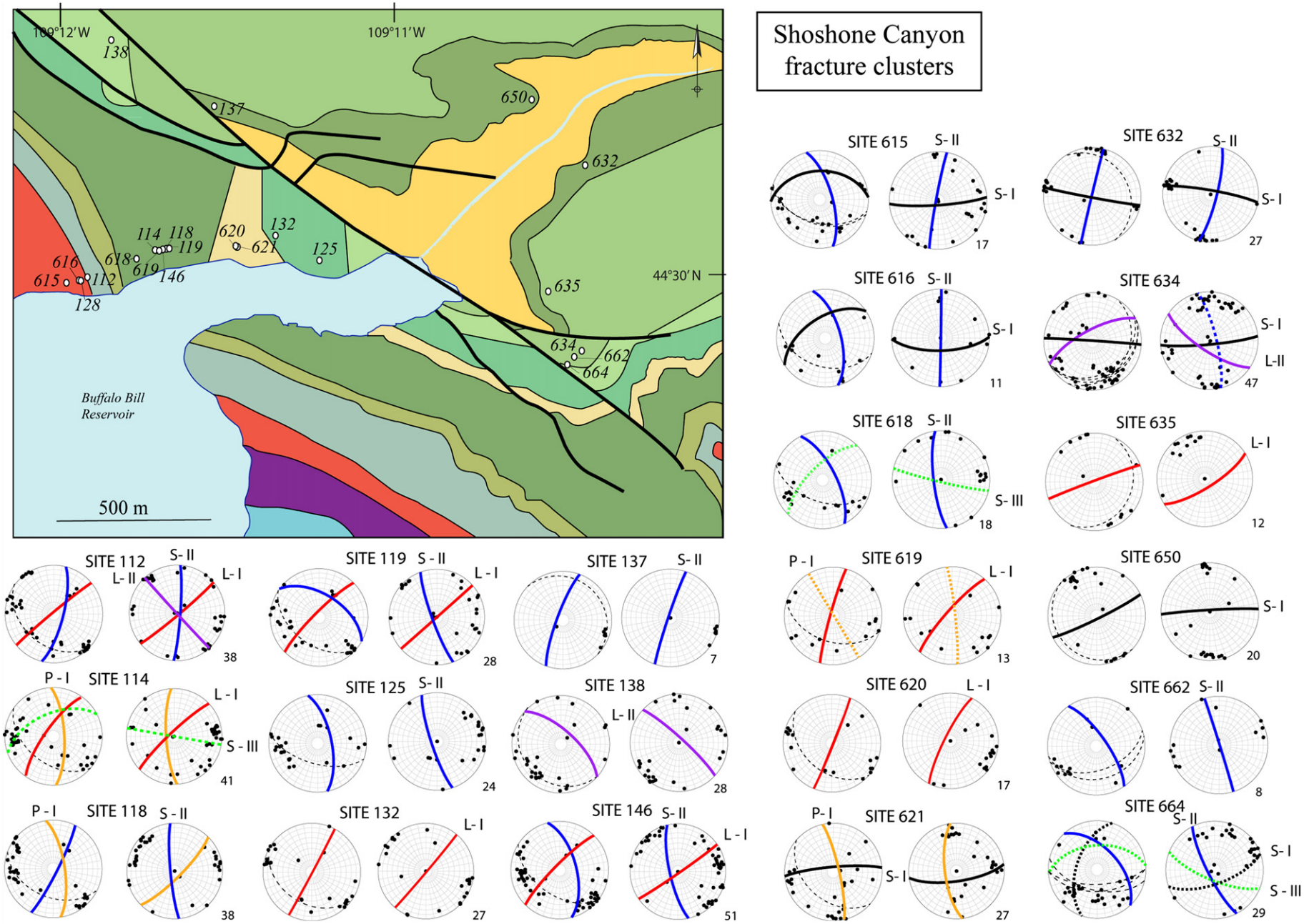

Fig. 11. Results of fracture analysis in the sedimentary cover in the Shoshone Canyon. Same keys as in Figs. 3 and 10.

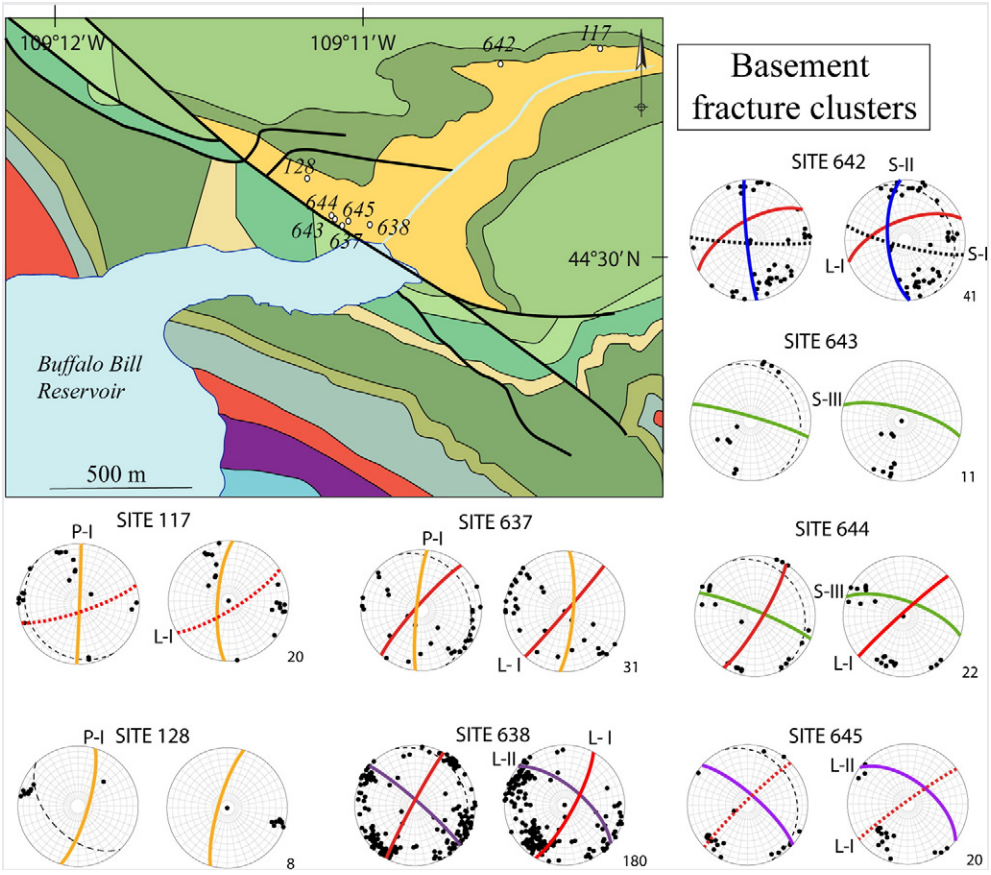

Fig. 12. Results of fracture analysis in the basement rocks in the Shoshone Canyon. Same keys as in Figs. 3 and 10.

Joints and veins striking 130°E (set L-II) abut on L-I joints and thus postdate them. Set L-II joints and veins are parallel to the fold axis; they are found in 18 sites, more abundantly near the basement thrust, thus near the hinge of the RMA, and in CM (Figs. 9a,d, 10–12). They developed in both cover and basement rocks, but none of these fractures were found in the forelimb of the RMA. In the other part of the folds, they strike 130°E near the hinge of the RMA and may rotate toward a 150°E trend further away in the backlimb of the RMA, where they are less abundant.

Another set, hereinafter named set L-III, is mainly made of reverse striated microfaults (Fig. 14), that developed under an horizontal σ_1 striking 035°E to 050°E in the current strata attitude.

The last fracture set includes joints and veins striking mainly N–S (020°E to 160°E) that are sub-vertical in the current (folded) strata attitude (set P-I, Figs. 10–12), and which cut across any other sets (Fig. 9f) except L-III. They are abundant in all the structural positions of both RMA and CM (15 sites of 49), they developed in all lithologies, in cover and basement rocks, with a remarkable vertical persistence. Unfortunately, we did not find any direct chronological relationships to determine which one of sets L-III or P-I is the oldest; nevertheless, as set L-III faults are consistent with the same contractional event than folding while P-I fractures are not, the latter is likely the youngest.

4.3. Results from fault–slip data inversion

The results of the inversion of fault–slip data for stress in the Shoshone canyon (the SE part of RMA) are presented in Table 2 and in Fig. 14, and compared to the data previously collected in 11 stations over RMA by Neely and Erslev (2009). Results comprise 11 sites, in which newly formed and/or reactivated fault data allowed reliable computation of both principal stress orientations and of the stress ellipsoid shape ratio, hence to completely define the local paleostress state.

Most stress tensors reveal a post-tilting contractional state of stress with a horizontal σ_1 oriented NNE to ENE with a mean 045°E trend (from 030°E in the Phosphoria Fm. to 050°E in the Madison Fm.), roughly perpendicular to the fold axis. This event is marked either by newly formed reverse faults mainly striking 130°E (Fig. 14, sites 131, 137, 125, 111), and strike–slip faults (Fig. 14, site 121). These features are observed everywhere regardless of the distance to the major basement fault and of the structural position within the fold. Preexisting E–W fracture planes reactivated as left-lateral/reverse strike–slip faults are also observed in the forelimb of the fold (e.g., Fig. 14, site 122).

Fault slip analysis also reveals two pre-tilting stress regimes. The first one corresponds to a horizontal σ_1 oriented 045°E near the basement fault (Fig. 14, site 118) and 020°E further away (Fig. 14, site 123). This stress regime is marked by either conjugate strike–slip faults (Fig. 14, site 118) or conjugate reverse faults (Fig. 14, sites 123, 131). In Cedar Mountain, the same strike–slip regime is also recognized, but with σ_1 oriented 060°E. The second pre-tilting state of stress, illustrated by site 132 (Fig. 14) but poorly encountered in our dataset, corresponds to a contractional/strike–slip regime with a sub-horizontal σ_1 oriented 115°E.

Finally, in the forelimb, widespread bedding-parallel slip is supported by slickenlines along bedding surfaces in the Bighorn, Phosphoria and Madison Fms. (Fig. 14, sites 111, 122, 131); although occurring obviously during fold amplification, bedding-parallel slip-related striated planes were represented, for the sake of simplicity, with the late-stage fold tightening related structures in the diagrams of Fig. 14.

4.4. Results from calcite twin analysis

The results of the inversion of calcite twins (Fig. 15, Table 3) were mainly obtained from veins filled with calcite from both limbs of the fold, in the limestones of the Mississippian Madison and Ordovician Bighorn Fms along with the sandstones of the Devonian Three-Forks Fm. The

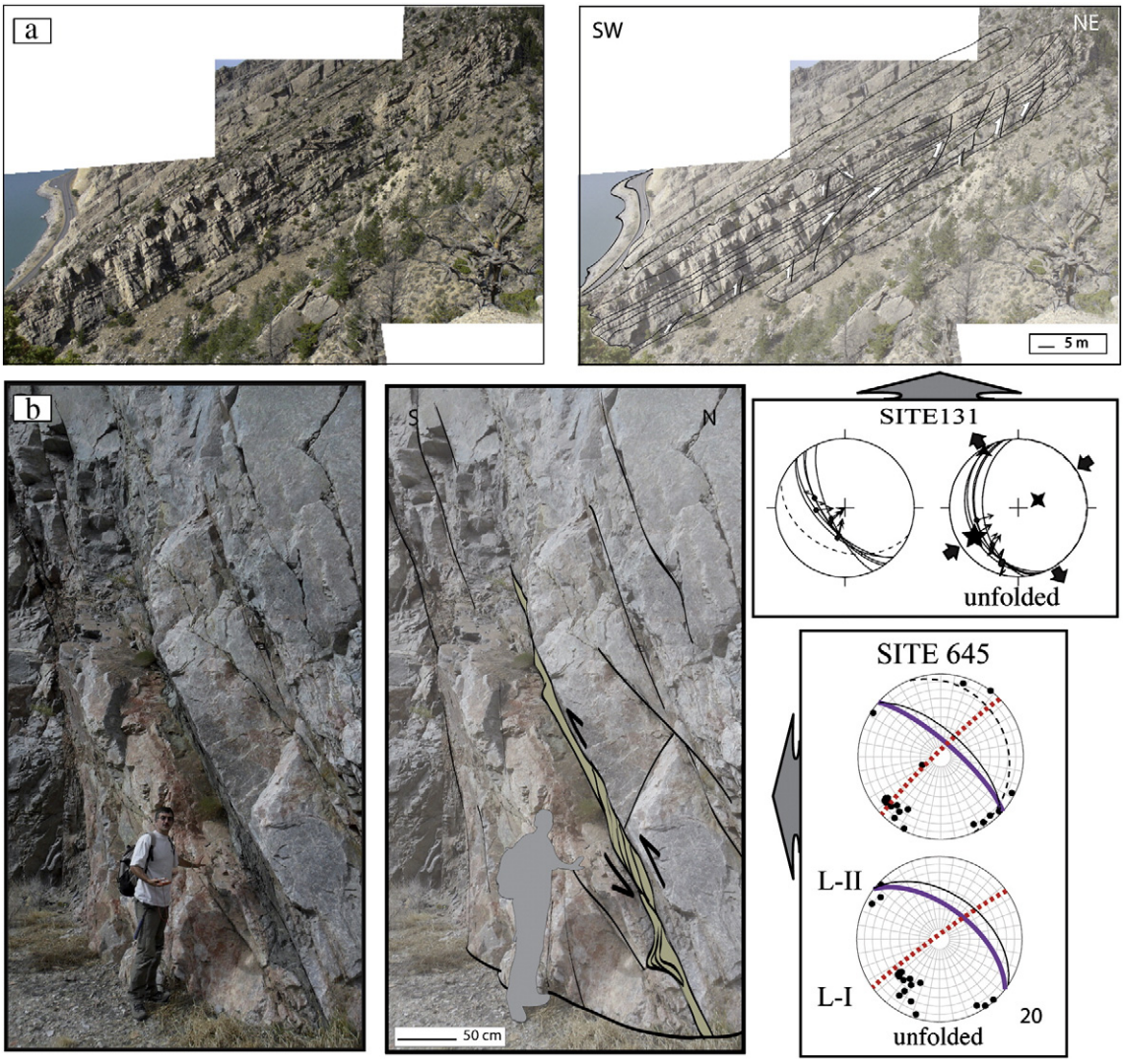

Fig. 13. –Photographs and interpretations of some fault systems observed at RMA, A- Early-folding fault network in the Ordovician limestone formation (Bighorn Fm.) in the forelimb. B- Example of a high-angle reverse fault, here filled with shaly gouges, in the Precambrian basement rocks. Note that this high-angle reverse fault (plane marked as black solid line on stereodiagrams) is parallel to major fractures planes within the basement. For stereodiagrams, same key as in Figs. 10–14.

degree of dolomitization of the Madison Formation was unfortunately too high to carry out systematic twin analysis from the rock matrix (Fig. 16a). In all the veins, internal deformation by twinning occurred under a thin-twin regime (Fig. 16), suggesting that temperature remained lower than 150–200 °C (e.g., Ferrill et al., 2004) and that internal strain by twinning did not exceed 3–4%. For each stress regime, differential stress magnitudes (σ_1–σ_3) were also computed (Table 3). The value of the critical resolved shear stress used for calculation of the differential stress magnitudes was selected according to both the internal twinning strain (e.g., twin density) and the mean grain size of the samples, as suggested by Rocher et al. (2004) and Amrouch et al. (2010a). Inversion of calcite twin data reveals 6 stress regimes (Table 3, Fig. 15).

The first pre-tilting twinning event is related to a contractional stress with horizontal σ_1 axis striking between 105° and 135°E; this stress regime was reconstructed from twinned calcite within bed-perpendicular veins striking 160°E and 030°E (Set S-II, samples SA04 and SC74, see discussion for details) and 130°E (Set S-III, sample SC82V1) (Fig. 15); related differential stress magnitudes (σ_1–σ_3) (vertical σ_3 axis) vary from 27 ± 5 MPa to 41 ± 8 MPa (Table 3).

The second pre-tilting event corresponds to a strike–slip regime with a horizontal σ_1 axis oriented 045°E recorded by twinned calcite in a bed-perpendicular veins striking 030°E (Set S-II, sample SC74), in two bed-perpendicular veins striking 165°E (Set S-II, sample R93) and 130°E (Set S-III, sample SC82V1) and in a bed-perpendicular vein striking 045°E (Set L-I, sample R62) (Fig. 15); differential stress magnitudes (σ_1–σ_3) (horizontal σ_3 axis) range from 34 ± 7 MPa to 49 ± 10 MPa.

A pre-folding stress tensor reconstructed in sample SC66V1 (i.e., from set S-II) shows a horizontal σ_3 axis striking 100°E but oblique σ_1 and σ_2 axes; because the stress ellipsoid shape ratio (Φ) close to 1 indicates close magnitudes of σ_1 and σ_2 hence likely stress permutations, this tensor probably reflects an extensional stress regime; the related differential stress magnitude (σ_1–σ_3) being 23 MPa.

An extensional stress regime with horizontal σ_3 oriented 050–060°E was recorded in veins striking 130°E (set S-III, sample SC82V1), 045°E (set L-I, sample R62), 150°E and 160°E (set L-II, samples SC58 and SC66V2) (Fig. 15); related differential stress magnitudes (σ_1–σ_3) (horizontal σ_3 axis) range from 23 ± 4 MPa to 38 ± 8 MPa.

A post-tilting stress regime has been reconstructed including both strike–slip and contractional stress regimes, with a horizontal σ_1 axis oriented from 020 to 065°E. The contractional regime was found in bed-perpendicular veins striking 150°E (set S-II, Fig. 15, sample SC58) with a differential stress magnitudes (σ_1–σ_3) (vertical σ_3 axis) of 29 ± 6 MPa. The strike–slip regime with differential stress magnitudes ranging from 31 to 74 MPa was reconstructed in veins striking 030°E (set S-II, 31 ± 5 MPa, sample SC66V1), 160°E (set S-II, 51 ± 10 MPa, sample SA04) (Fig. 15), and in the matrix of sample R62 (74 ± 13 MPa).

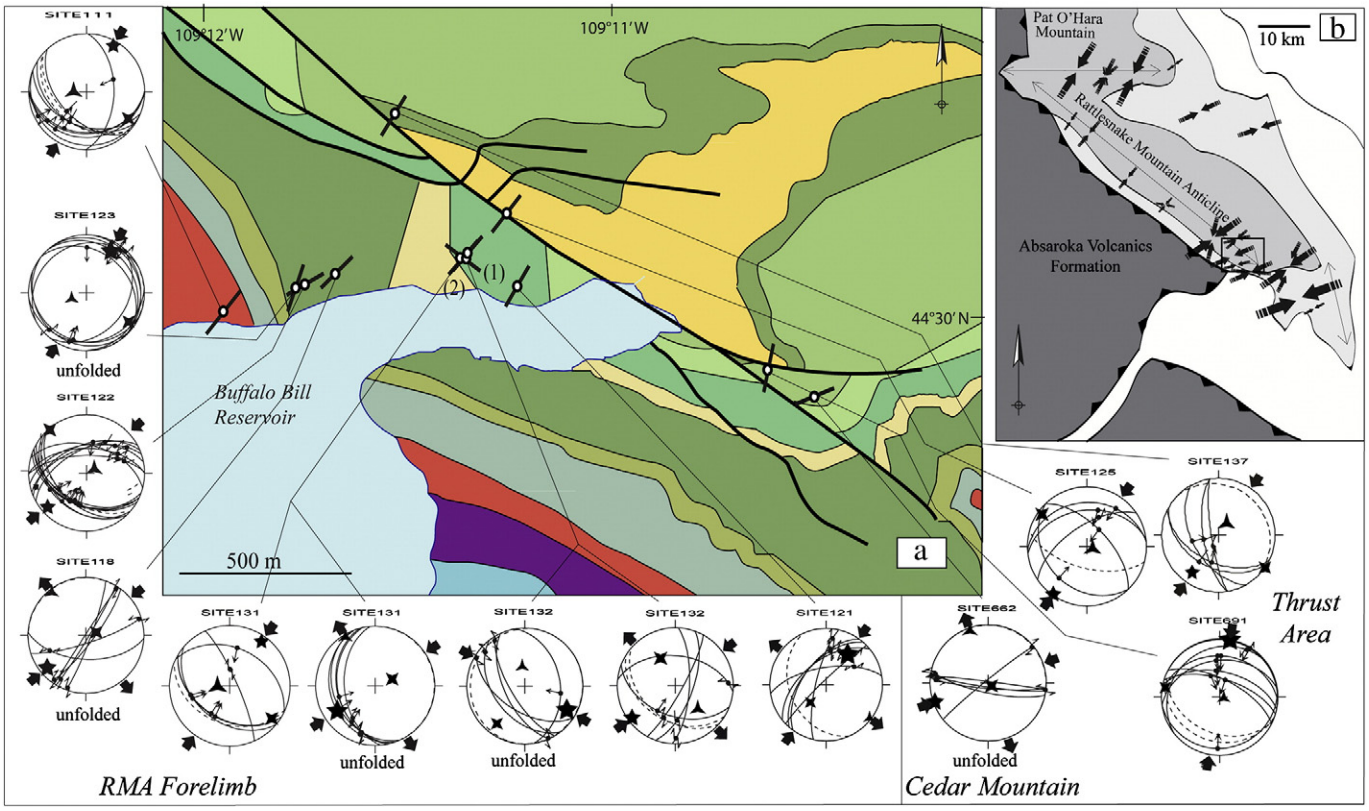

Fig. 14. a – Results of fault–slip data inversion (Schmidt's stereonets for each site localized nearby the Shoshone canyon, map location shown in Fig. 10). Computed stress axes are reported as stars with three branches (σ_3), four branches (σ_2) and five branches (σ_1). Black arrows indicate direction of compression if convergent or extension if divergent. Maximal horizontal stress trends are reported as sticks on the geological map, with chronological sequence as (1)/(2), from the oldest to the youngest. Bedding-plane is shown as dashed line on stereodiagrams where data are in their present-day attitude. 'Unfolded' refer to unfolded data. B - Map showing compressional trends inferred from the study by Neely and Erslev (2009). Size of arrows is proportional to the number of data used. Modified after Neely and Erslev, 2009.

Finally, a post-tilting extensional stress regime with a horizontal σ_3 axis oriented 075° to 100°E has been determined from two veins striking 050°E (set L-I, sample R297) and 160°E (set P-I, sample SC82V2) (Fig. 15) with differential stress magnitudes (σ_1–σ_3) (horizontal σ_3 axis) ranging from 37 ± 7 MPa to 56 ± 11 MPa. This regime postdates the opening of the 050°E vein and likely reflects the opening of the 160°E vein.

5. Interpretations and discussion

5.1. Kinematics of Laramide basement-cored folds

A commonly admitted kinematic interpretation of Rattlesnake Mountain is that the deformation of the cover is consistent with the trishear model (Erslev, 1991; Johnson and Johnson, 2002). The trishear

Table 2
Paleostress tensors computed from inversion of fault slip data.

Site	Formation	Bedding strike-dip	Trend (plunge) of the principal stress axes (degree)			Ratio between differential stresses φ	Number of data	Quality indice
			σ_1	σ_2	σ_3			
111	Phosphoria	131–41S	30 (9)	123 (16)	270 (72)	0.6	8	B
118	Madison	113–45S	236 (40)	358 (14)	83 (47)	0.2	6	B
			230 (14)[a]	74 (75)[a]	322 (6)[a]			
121	Bighorn	156–35W	36 (35)	225 (54)	129 (4)	0.1	6	A
122	Madison	129–57S	228 (12)	319 (3)	66 (77)	0.6	11	B
123	Madison	133–64S	206 (44)	298 (2)	30 (46)	0.2	9	B
			39 (21)[a]	251 (66)[a]	133 (12)[a]			
125	Bighorn	105–60S	215 (2)	305 (8)	111 (82)	0.6	5	A
			35 (10)	128 (13)	267 (73)	0.7	6	A
131	Bighorn	113–37S	258 (52)	44 (33)	145 (16)	0.2	6	C
			236 (24)[a]	68 (65)[a]	328 (4)[a]			
			224 (16)	326 (38)	116 (48)	0.2	10	B
132	Bighorn	122–39S	108 (12)	221 (59)	12 (27)	0.2	6	A
			120 (18)[a]	217 (20)[a]	352 (62)[a]			
137	Flathead	134–15N	228 (18)	318 (0)	49 (72)	0.7	6	B
662	Grosventre	102–33S	291 (43)	192 (9)	93 (45)	0.3	5	A
			250 (3)[a]	131 (84)[a]	341 (5)[a]			
691	Grosventre	114–38S	184 (0)	274 (6)	94 (84)	0.5	9	A

Quality indice determined according to numerical estimators such as the angle between computed shear stress and actual striation.
[a] Unfolded stress axes.

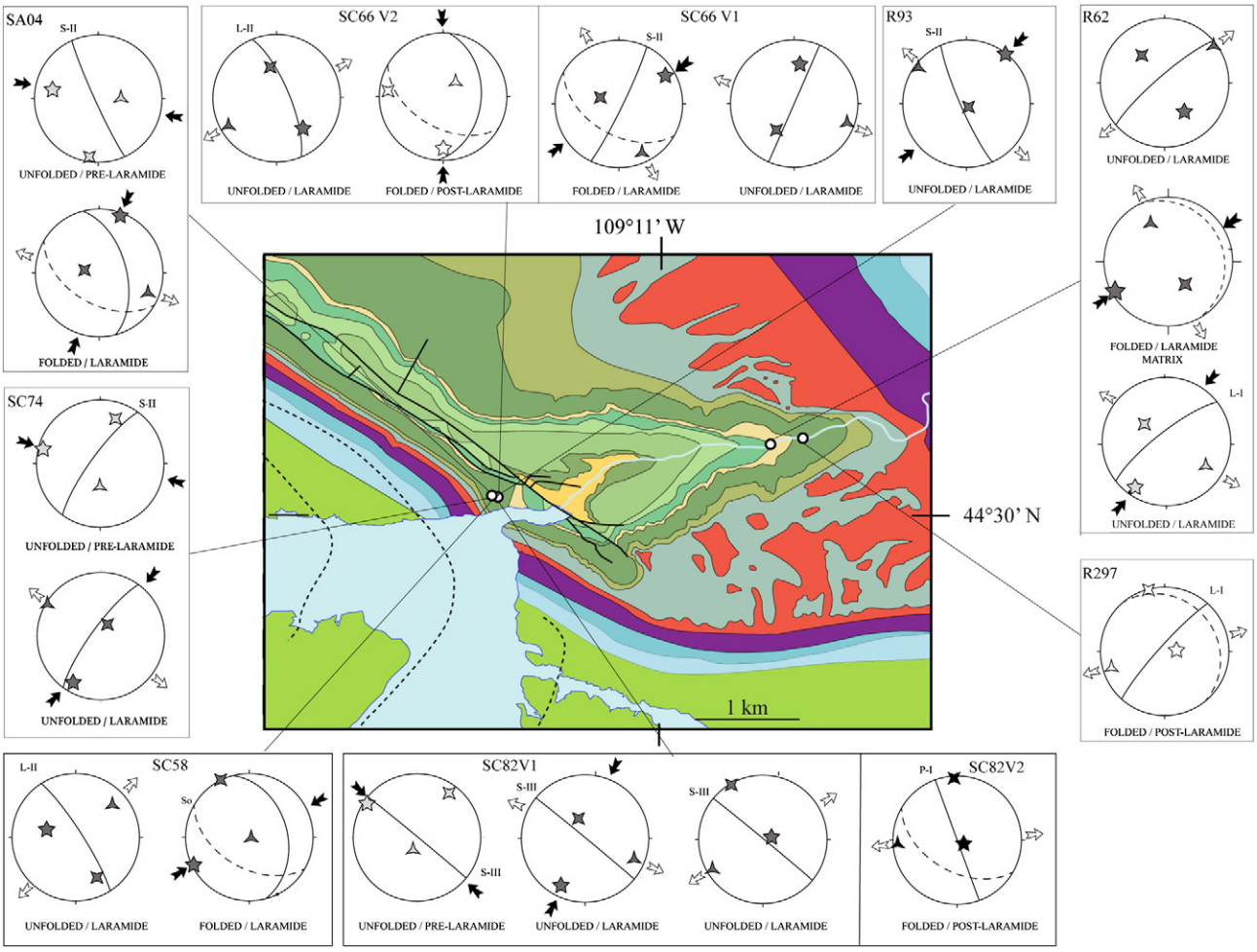

Fig. 15. Paleostress orientations reconstructed from calcite twinning (Schmidt's stereonets). The folded/unfolded attitude of the principal stress axes is reported, together with the related tectonic event. Light grey symbols refer to pre-Laramide events, dark ones refer to Laramide events and white ones to post-Laramide events. Black/white arrows indicate directions of compression/extension.

model is a kinematic model used to replicate the curved fold surface above a propagating thrust. It is defined as a triangular shear zone wherein the deformation is distributed. According to Erslev (1991), the apex of the triangular shear zone is usually located at the cover/basement interface, while Bump (2003) considers that, in some cases, this apex may be located below this interface, at the tip of the propagating fault.

According to our new field observations, we proposed cross-sections involving an overturned forelimb of RMA and steep reverse faults in the cover. The cumulative displacement profile along RMA and CM exhibits a single D-max, located in the northwest part of RMA (Fig. 8). Thus, it suggests a sequential development of folds during the Laramide contractional event, with CM developed later than RMA, but in the same phase of deformation. If CM had developed early and/or if RMA had propagated from CM thrust, the D-max would have been located at the thrust intersection (see for example Bellahsen and Daniel, 2005; Bellahsen et al., 2006c and references therein). It also suggests that all the thrusts involved in the basement wedge were active coevally. These finite geometry and kinematics may be considered as similar to a trishear model, as a triangular zone with distributed faults is similar to a distributed shear zone. However, the coeval timing of propagation of the fault-splays implies the existence of an early triangular shear zone in the basement (Fig. 17 a, step 1:"immature stage"). The apex of such a zone would thus be located deeper than the basement top. In the trishear model, this would imply that the thrust upper tip was located beneath the basement top, as suggested in Bump (2003), before propagating toward the surface. In the case of RMA, the basement is (pre)cut by several inherited fault populations, with various orientations. Moreover, it has been proposed that RMA resulted from the reactivation of a basement weakness (Erslev and Koenig, 2009). Such result is actually confirmed by the Dmax/L ratio (typical of a reactivated fault, see above). Thus, the upper tip of the inherited fault was most probably, as early as the onset of faulting, at the basement-cover interface. In such a case, the triangular shear zone in a trishear model cannot explain the zone of distributed faulting in the basement, as in trishear the distributed deformation zone only develops above the upper fault tip. An alternative explanation must then be found for the inferred deformation distributed on several fault planes in the basement (see similar considerations in Bellahsen et al., 2006b).

On our balanced sections, the switch from localized to distributed faulting is set few kilometers below the basement-cover interface. The reasons for such a switch remain unclear, but hydration of upper basement rocks could explain a change in rheology and thus a distribution of brittle deformation. The occurrence of such a zone of hydration of the basement rocks has been documented (e.g., Boiron et al., 2003; Cathelineau et al., 2004; Essarraj et al., 2005; Fourcade et al., 2002; Mercadier et al., 2010) and has been related to basement alteration and/or exchange with basinal fluids (mainly brines at the basement/cover interface in foreland basins).

According to Amrouch et al. (2010a), the deep structure of SMA is interpreted with the similar basement geometry than RMA, including a steep reverse fault and a fault splay underlying the sedimentary

Table 3
Paleostress tensors computed from inversion of calcite twin data.

Sample	Formation	Bedding Strike–Dip	Vein Strike–Dip	Trend (plunge) of the Principal Stress Axes (degree)						Differential Stress ($\sigma1 - \sigma3$)* (MPa)	Ratio Between Differential Stresses Φ	Total Number of Data (T/UT)	Number of Data Consistent With the Tensor T/UT
				σ1		σ2		σ3					
SA04	Madison	120–50SW	165–55E	20	4	279	71	111	19	51	0.5	162/78	64/78
			155–88E*	312	30	174	52	55	21	27	0.5	101/78	42/78
				282	27*	189	7*	86	62*				
SC58	Madison	120–50SW	165–40E	339	38	114	42	228	25	38	0.3	127/47	50/47
			147–81E*	286	51*	152	29*	48	23*				
				244	3	154	0	60	87	29	0.3	77/47	32/47
R93	Madison	123–43S	161–62E	230	41	27	47	130	11	49	0.5	147/78	67/78
			156–82W*	38	2*	149	85*	308	5*				
SC74	Madison	120–50SW	25–78W	213	67	30	23	121	1	42	0.4	219/81	87/81
			32–80W*	211	17*	30	73*	301	0*				
				297	17	200	23	60	61	41	0.5	132/81	46/81
				285	9*	20	26*	179	62*				
SC82V1	Madison	120–50SW	135–40NE	39	31	142	21	261	51	39	0.7	218/61	82/61
			130–89NE*	72	78*	330	2*	240	11*				
				126	1	216	35	35	55	33	0.4	136/61	62/61
				305	4*	35	15*	199	75*				
				203	69	9	20	100	5	34	0.5	74/61	35/61
				207	19*	342	63*	111	19*				
SC82V2	Madison	120–50SW	160–90*	194	83	12	7	102	0	56	0.6	112/38	62/38
SC66V1	Madison	120–50SW	26–85E	59	16	289	65	154	18	31	0.5	156/78	68/78
			30–88W*	193	9	14	81	283	0	23	0.9	88/78	36/78
				8	39*	214	49*	109	13*				
SC66V2	Madison	120–50SW	05–40E	99	36	5	6	267	54	31	0.4	287/133	109/133
			342–76E*	139	37*	350	49*	241	16*				
				180	21	276	15	39	64	31	0.5	178/133	67/133
R62	Bighorn	152–15NE	52–78W	216	3	309	49	123	41	34	0.4	167/76	76/76
			46–82W*	214	16*	327	53*	114	33*				
				159	45	306	40	51	18	23	0.4	91/76	38/76
				144	45*	319	45*	51	3*				
			Matrix	61	6	143	54	155	35	74	0.3	64/44	32/44
R297	Madison	140–19N	42–83W	86	75	345	5	254	15	37	0.5	177/69	70/69

cover (see SMA cross section in Fig. 17b). Despite a lack of geophysical imagery, the location of the steep reverse splay at SMA has been reliably constrained by paleohydrological studies in the cover rocks, supporting the occurrence of a hydraulic conduit in the basement just below the backlimb (Beaudoin et al., 2011). We thus assume that SMA illustrates a less mature stage of thrust-related, basement-cored fold compared to RMA (Fig. 17b). The difference of maturity between SMA and RMA has already been suggested by Katz et al. (2006). Indeed, their stable isotopic studies show that the fluids involved in the paleohydrological system of SMA had less chemical exchanges with the granitic basement of the region than in other larger folds (namely RMA), suggesting less displacement along the main basement thrust underlying SMA or less extended vertical connectivity of the reservoir fracture network (Barbier et al., 2012a).

A unified growth model for Laramide-type thrust-related anticlines is proposed here (Fig. 17a), based on the assumption that RMA is more mature than SMA, and that the synchronism of the faults at RMA is also valid for the faults at SMA. The main differences between SMA and RMA are (1) the presence of a large basement wedge in the footwall of RMA (Erslev, 1995), which is related hereinafter to the larger amplitude of RMA, and (2) the position of these folds, SMA being an arch backlimb while RMA is an arch forelimb (Neely and Erslev, 2009). Considering a structure similar to SMA, *i.e.* in an immature stage, the coeval propagation of the basement thrusts will increase displacement along faults, implying significant syn-folding erosion, in agreement with the findings of Amrouch et al. (2011). As proposed above, if one considers that the depth of the transition from localized to distributed deformation in the basement is related to the thickness of a zone of hydration of the basement (or to any other processes), thus one can consider that this depth is constant (at about few km). Then, the increase in exhumation and erosion will move downward (relatively to the top of the basement hanging-wall) the apex of the triangular shear zone (to stick to the transition depth), increasing the thickness of basement rocks affected by deformation (Fig. 17a, step 2- "Mature stage"). This large basement wedge comprises several reverse faults that accommodate deformation in a brittle way, the lowest being the youngest. During the late evolution however, when the lowest thrusts were activated, the upper ones (i.e. the oldest) propagated into the cover (Fig. 17a), cross-cutting the sub-vertical forelimb of RMA (as shown in Fig. 4).

As a matter of fact, our model does not account for the cessation of the evolution of SMA, which might be due to the fact that SMA is a back-thrust soled shallowly on the Rio Thrust (Fig. 17b), meanwhile RMA is a fore-thrust soled much deeper in the crust (e.g. Neely and Erslev, 2009).

5.2. Fracture pattern evolution

To constrain the paleostress evolution in space and time at both the local and the regional scales and their relationships with fracture development, field observations have been compared and combined with paleostresses independently reconstructed from striated faults and calcite twins. The 7 fracture sets described in Section 4.2 can be related to 3 regionally significant tectonic events, each being associated with various stress regimes (Figs. 18 and 19). The relative chronology of the different twinning events and related paleostresses was established by considering that the attribution of a vein to a fracture set must be consistent with the stress tensors recorded by twinned calcite filling this vein. In other words, the stress tensors recorded in twinned calcite of a vein must either be coeval or postdate the opening of the studied vein and its set. This independent chronology was used in turn to refine the range of orientations of the fractures defining each set (Section 4.2). In most samples however, calcite twinning-derived stress tensors confirm the previously

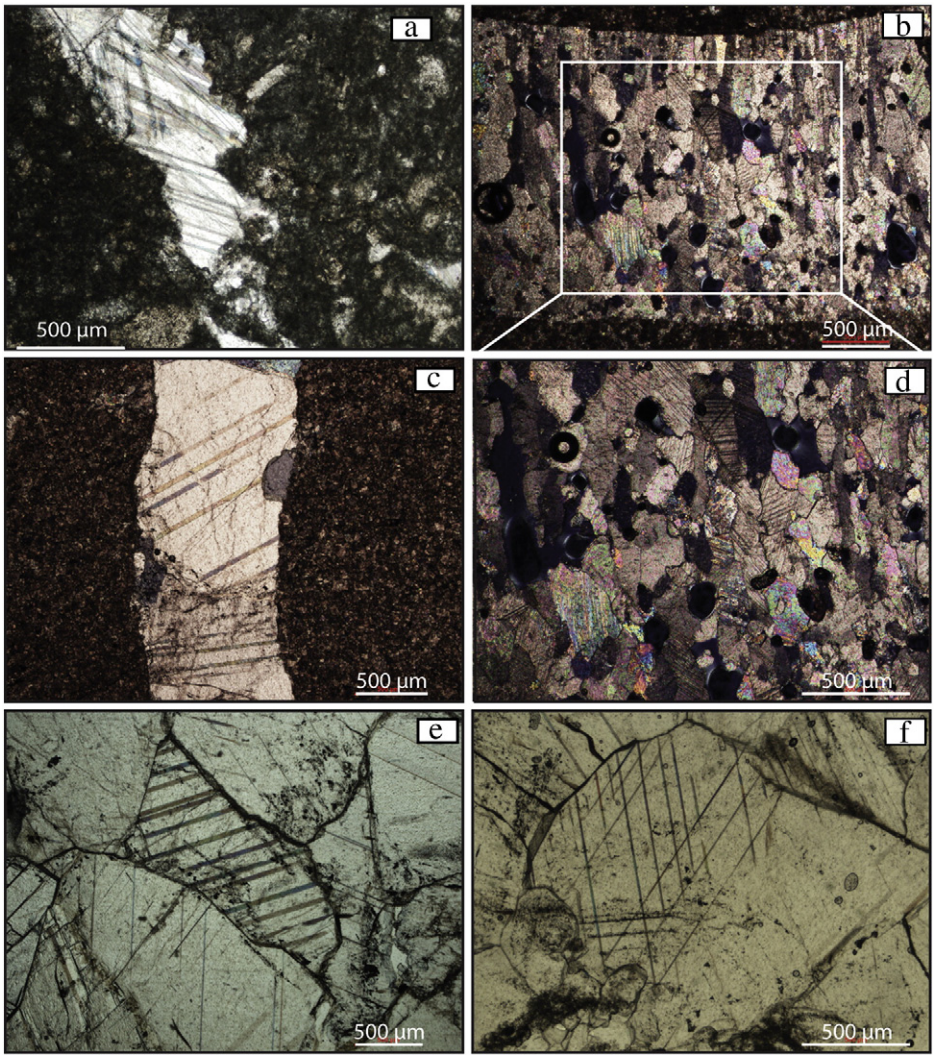

Fig. 16. Photomicrographs of thin sections observed under polarized light exhibiting thin calcite twins in the matrix (sample R62 (a)) and in veins of samples R297 (c), SC74 (b, d), SC 58 (e) and SC 82 (f).

defined sequence of fracture development. Thus, fracture sets could reliably be related either to pre-Laramide (Sevier) contraction, to the Laramide contraction or to a post-Laramide extensional tectonic event.

5.2.1. Sevier-related fractures

The oldest fracture set comprises joints striking 060°E to 090°E. Nonetheless, this bed-perpendicular set S-I strikes mainly E–W, and predates every other sets (Fig. 9); it could be related to an early Sevier contractional event (Fig. 19a), with a nearly E–W compressional trend consistent with earlier studies showing that the orientation of Sevier related σ_1 in western Wyoming was oriented E–W (Fig. 1-c; Bird, 1998; Craddock, 1992; Craddock and Van der Pluijm, 1999).

The set S-II joints (striking mainly N–S) have been observed in different areas of the Bighorn basin (defined as "set N–S", Amrouch et al., 2010a). At RMA, joints and veins composing this set strike N–S to 30°E (Fig. 15, sample SC74). This fracture set postdates set S-I and predates S-III as suggested by macroscopic observations and calcite twin analysis. Indeed, a tensor with a σ1 axis oriented WNW–ESE (consistent with the formation of S-III veins) was reconstructed in a vein striking 150°E (Fig. 15, SA04), which suggests that the 150°E vein belongs to a set that formed prior to set S-III. This implies that this 150°E vein belongs to set S-II. We propose that this set S-II that formed before the Laramide orogeny, and therefore during the Sevier orogeny, reflects a roughly E–W extension recorded at the basin scale, as also illustrated in calcite twins of sample SC66. This extension could tentatively be related to the flexure of the Sevier foreland during the late Cretaceous (DeCelles, 2004), leading to opening of widespread veins striking mainly N–S to NNE–SSW (Fig. 19b), marginally opening veins oriented from NNE–SSW to NNW–SSE (see similar foreland flexure-related features and considerations in Billi and Salvini, 2003; Lash and Engelder, 2007; Quintà and Tavani, 2012-this issue).

The pattern of set S-I and set S-II are sometimes similar to a pattern intermediate between a ladder pattern and a grid pattern, as defined by Rives et al. (1994) for orthogonal cross-joints (Fig. 9b). Indeed, S-II may be cross-joints developed during the development of set S-I (see pattern in Fig. 9b), implying a stress permutation mechanism (Bai et al., 2002). In such a case, set S-II would not represent a distinct fracturing event with respect to set S-I. However, in most cases, S-II joints consistently abut on S-I joints. Moreover, set S-I fractures were observed at sites where S-II fractures do not exist; the opposite case was also observed (see Fig. 10, sites 125, 650 for instance). Thus, both sets most probably reflect two distinct far-field stress states, as considered below.

Striking 110°E to 130°E, S-III fractures opened in mode I, under a strike–slip regime (horizontal σ_1 and σ3 axes). However, calcite twinning data reveals a compressive stress regime with a horizontal

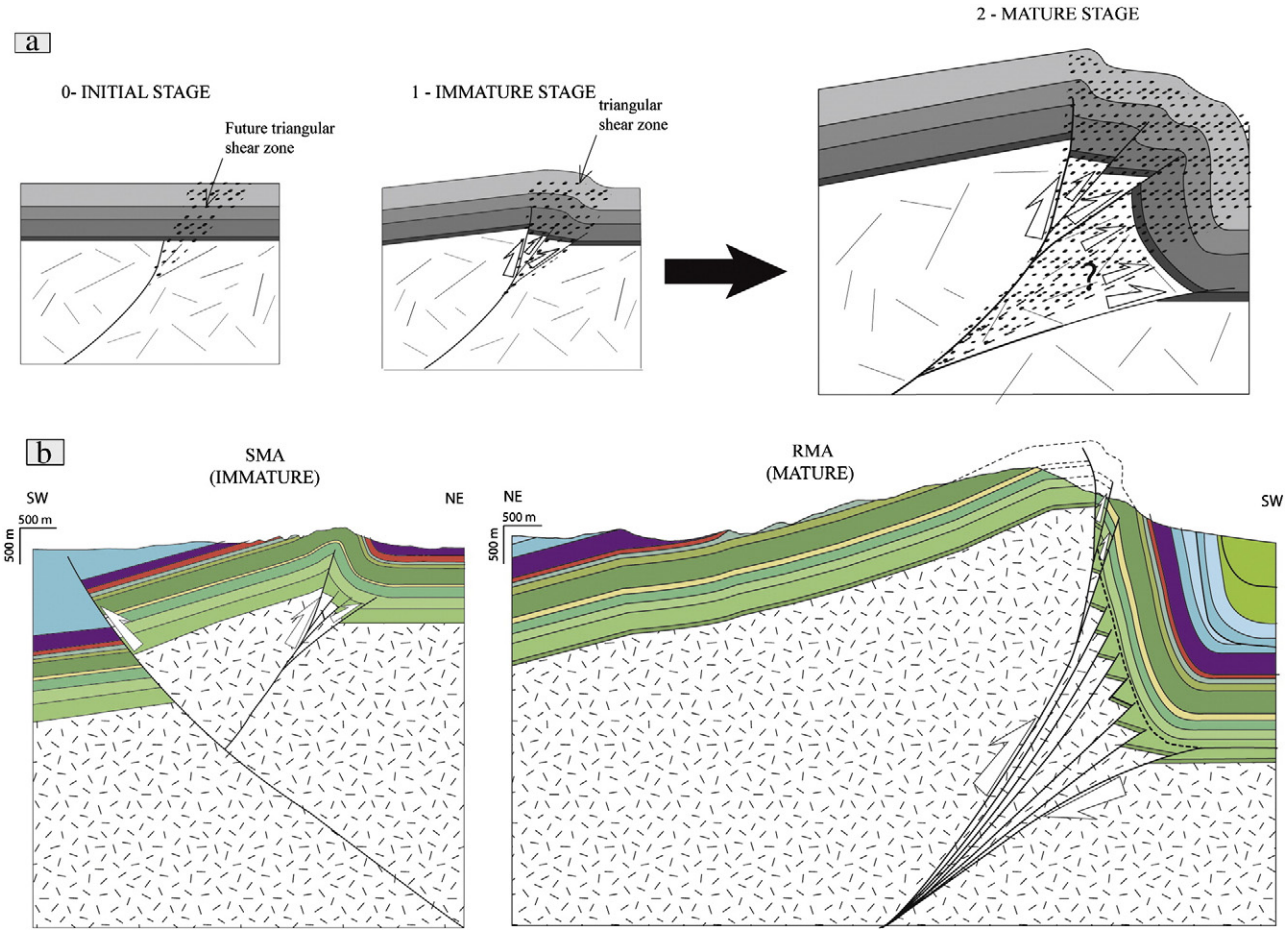

Fig. 17. a - Conceptual model of fold growth for the Laramide basement-cored folds. The spotted area represents the location of a triangular zone of shear distribution both in the basement and in the cover. b - The two growth steps highlighted in the model are represented along with actual structures of natural analogs of the Bighorn basin: the Sheep Mountain Anticline and the Rattlesnake Mountain Anticline.

Fracture set	Mean strike of fractures	Paleostress from fractures	Paleostress from striated microfaults	Paleostress from calcite twins	Related Tectonic events	
Set S-I	090°E to 060°E	σ_3 σ_1			Sevier layer-parallel shortening	Pre-Laramide
Set S-II	180°E to 020°E	σ_3			Formation of the flexural foreland basin	
Set S-III	110°E	σ_3 σ_1	σ_1	σ_1	Sevier layer-parallel shortening	
Set L-I	045°E	σ_3 σ_1	σ_3 σ_1	σ_1 σ_3	Laramide layer-parallel shortening	Laramide
Set L-II	135°E	σ_3		σ_3	Local curvature-related extension	
Set L-III	045°E		σ_1	σ_1 σ_3*	Late stage of fold tightening	
Set P-I	180°E to 160°E	σ_3		σ_3	Basin and Range extension	Post Laramide

Fig. 18. Sequence of fracture development derived from field observations, together with results of the analyses of calcite twin data and fault–slip data in terms of stress, and interpretation in term of tectonic event. *: stress axes close to permutation.

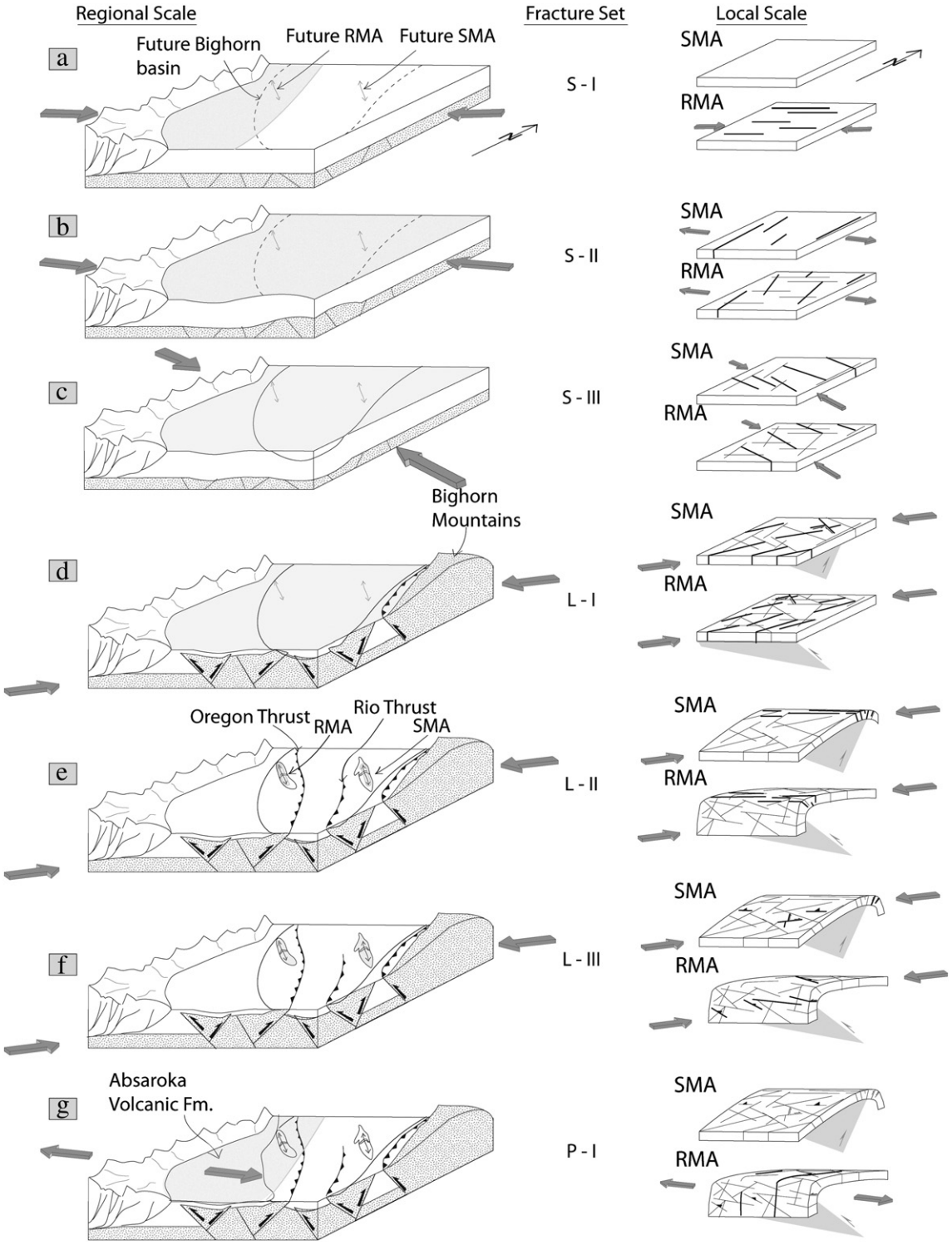

Fig. 19. Schematic evolution of tectonic regimes in the Bighorn basin and related fold-fracture relationship at Rattlesnake Mountain and Sheep Mountain anticlines. Gray patterns on the diagrams represent the geographic zones wherein related fracture sets developed.

σ_1 axis striking between 110°E and 135°E (Fig. 15, sites SC82, SA04, SC74) and a nearly vertical σ_3 axis. This suggest the occurence of stress permutations during the WNW–ESE compression, consistent with the low Φ ratio of 0.2 reconstructed from fault–slip data inversion (Table 2). This stress regime is mechanically and kinematically consistent with some bed-perpendicular stylolites observed in thin sections and with few striated faults (Fig. 14, site 132) marking a pre-folding WNW–ESE compression. S-III at RMA strongly resembles the pre-Laramide "set I" defined at SMA (Bellahsen et al., 2006a) tentatively related to the Sevier contractional event (Fig. 19c, Amrouch et al., 2010a) with a horizontal σ_1 axis also striking 110°E to 135°E (Fig. 1-c). Calcite twins in vein 1 of sample SC82 (Fig. 15), striking 140°E, yield a stress sequence from late Sevier to Laramide, which suggests that this vein could belong to S-III. Thus, the difference in strike between the compressional trends controlling the formation of S-I and S-III sets reflects two different LPS phases during the Sevier contractional history: an early Sevier contraction oriented E–W forming fractures of set S-I (Sevier LPS-1, Fig. 19a)

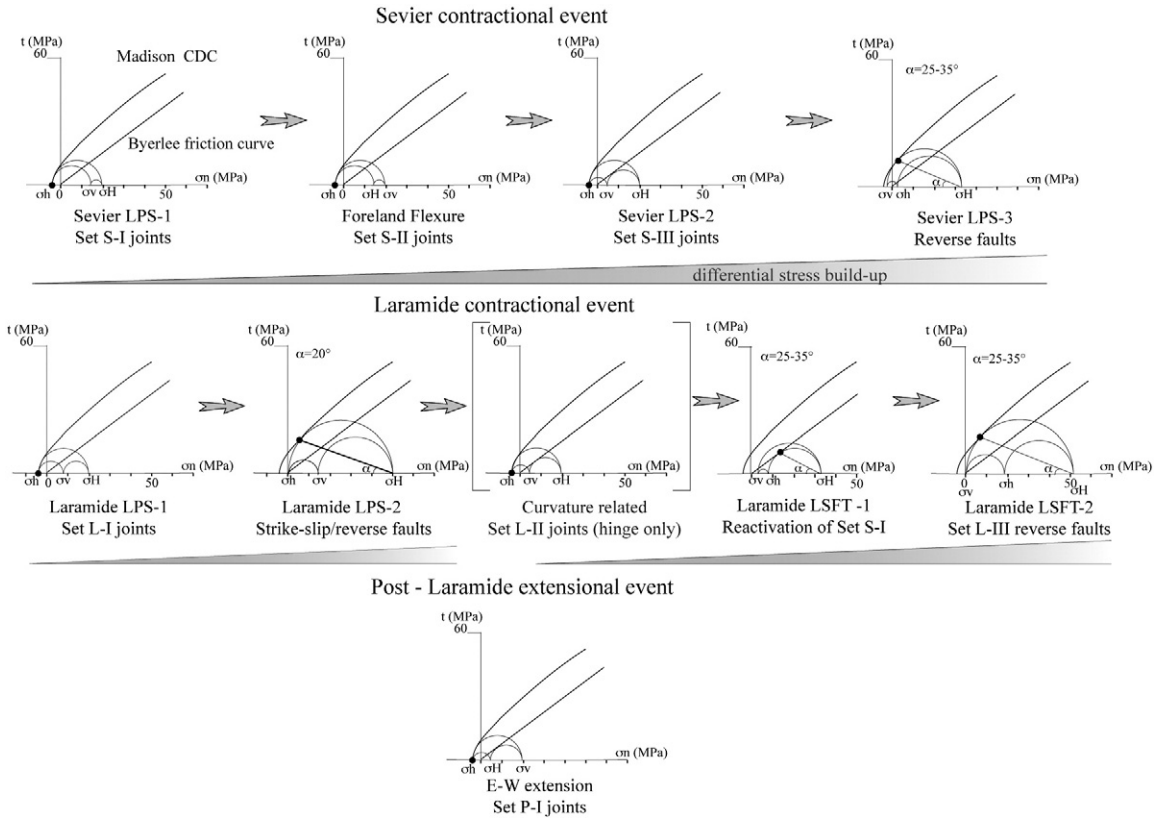

Fig. 20. Mechanical scenario of fracture development at Rattlesnake Mountain Anticline. Differential stress magnitudes were computed from calcite twinning paleopiezometry; Mohr circles were fit with failure/friction curves according to the geometry/kinematics of minor faults and/or the geometry/opening modes of fractures (see Amrouch et al., 2011). For each deformational sub-stage, this Mohr construction yields order of magnitudes of principal stresses and their evolution through time (see text).

which evolved through time into a WNW–ESE to NNW–SSE contraction forming the fractures of set S-III (Sevier LPS-2, Fig. 19c).

5.2.2. Laramide-related fractures

Fractures of set L-I are consistent (and likely coeval) with some early-folding strike–slip faults (Fig. 14, site 118) along with some calcite twin sets yielding paleostress tensors of strike–slip type (Fig. 15, sites SC74, SC82, R93) with a horizontal σ_1 axis oriented mainly 040°E to 060°E (Fig. 14, Site 662). The range of reconstructed σ_1 trends is in very good agreement with the result of the study of Neely and Erslev (2009), who highlighted a range of shortening directions from N–S to E–W (as reported in Fig. 14) with a mean shortening direction of 040°E at RMA, despite a rather 065°E regional trend. These authors explained the 040°E local trend by a reorientation of the 065°E regional stress related to the faults underlying RMA and CM. In line with this, our whole data set further shows that this local shortening 040°E trend mainly predates folding, as in SMA (Amrouch et al., 2010a). Thus, this confirms that compressional stresses where reoriented as early as during the Laramide LPS stage, possibly in response to stress perturbations above the basement faults (Neely and Erslev, 2009), as already suggested in Bellahsen et al. (2006b) and Amrouch et al. (2010a, 2011) for SMA.

As a matter of fact, set L-I fractures likely reflect LPS (including early-folding shortening) during the Laramide event (Fig. 1-d, Craddock and Van der Pluijm, 1999; Neely and Erslev, 2009; Varga, 1993, Fig. 19d). The occurrence of some reverse faults during that stage (Fig. 14, sites 131, 123; Fig. 13A) again suggests permutations between σ_2 and σ_3 axes.

Set L-II joints can be related to the syn-folding curvature of strata because they strike parallel to the fold axis and are more abundant near the hinge of RMA (Fig. 19e). Moreover, results from calcite twin study reveal an extensional stress regime with horizontal σ_3 axis striking perpendicular to the fold (Fig. 15, samples SC66, SC74, SC82, SC58). L-II joints reflect the way internal strain is accommodated at the fold hinge while bedding-parallel slip prevails in fold limbs.

In our results, we found no clear evidence for stress tensors with maximum compression axes inclined consistently less than, but in the same direction as bedding dip which would have reflected syn-folding twinning or faulting (e.g., Harris and Van der Pluijm, 1998; Lacombe, 2001). Concerning the fractures, those striking perpendicular to bedding strike (L-I) may be interpreted as occurring during any stage of fold growth, hence syn-folding *sl.* Tavani et al. (2006) argued that micro/mesostructures (bed-perpendicular joints/stylolites, and more generally faults and calcite twins) that yield maximum compression axes inclined consistently and with the same dip as the bedding and interpreted as early-folding may have developed within already tilted layers (syn-folding *ss*) if bedding anisotropy was able to significantly reorient stresses or if flexural slip occurred at very low friction so that the principal stresses rotated but remained either parallel or perpendicular to bedding. We do not rule out this possibility for L-I fractures, keeping however in mind that this may occur for a very small range of low bedding dips (e.g., Callot et al., 2010), and has not been documented for steeply dipping strata (and seems unlikely as well). It is however not relevant for many of our data (S-I, S-II and S-III), for which a number of abutting/cross-cutting relationships between fractures unambiguously support that they developed before the L-I sequence, hence are pre-Laramide. Since set L-II is syn-folding as confirmed by the comparison with neighboring locations where similar features are recognized, as in SMA (Amrouch et al., 2011; Bellahsen et al., 2006a), it seems reasonable to interpret the sets S-I to L-I that predate L-II as mainly pre-tilting.

The Laramide event is also marked by Set L-III newly formed faults, witnessing both contractional and strike–slip stress regimes, with σ_1 mainly striking 040°E in RMA (Fig. 14) leading also a reactivation of S-I

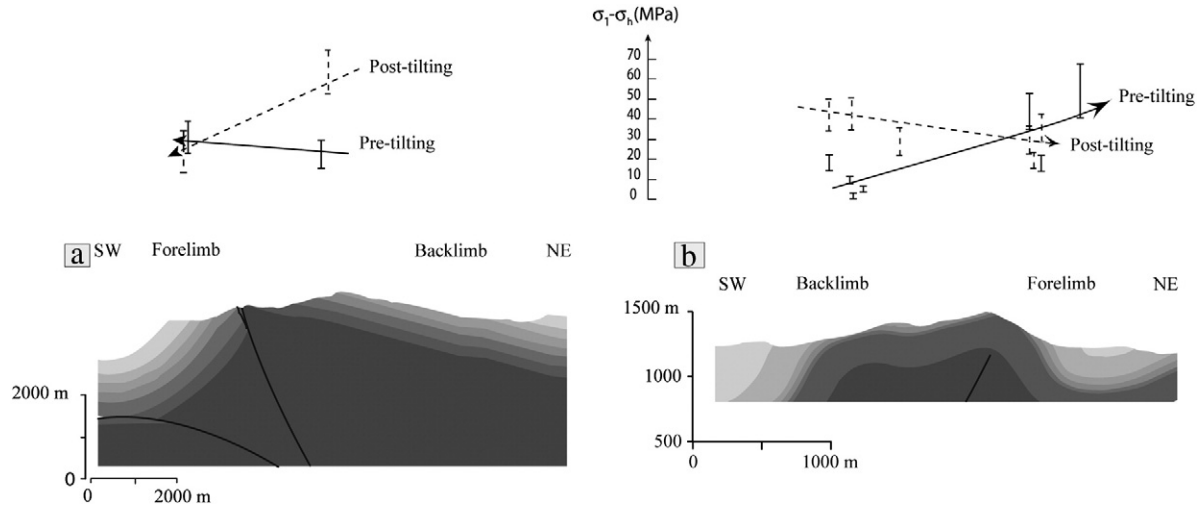

Fig. 21. Evolution of Laramide early-folding (LPS-related) and late-folding (LSFT-related) differential stresses (σ_1–σ_h) (strike–slip regime) across Rattlesnake Mountain anticline (a) compared with Sheep Mountain anticline (b, Amrouch et al., 2010a). Values of differential stresses at RMA have been calculated for a burial depth equivalent to SMA by applying calculation after Lacombe, 2007 considering an hydrostatic pore pressure gradient, a friction coefficient of 0.6 and a differential burial depth of 0.6 km. For RMA, sites have been projected perpendicularly on the cross section D–D' of Fig. 6.

fractures as reverse/strike–slip faults in the forelimb (Fig. 14, site 122). An exception appeared at the Cedar Mountain site (Fig. 14, site 691), which exhibits a horizontal σ_1 axis striking 010°E, i.e. nearly perpendicular to the E–W strike of a minor fault nearby the location of the site. Thus, this 010°E compression can be related to the same Laramide contraction and likely reflects a stress perturbation nearby the fault. Calcite twin data and fault–slip data yield both strike–slip and compressive states of stress, with horizontal σ_1 axis oriented 040°E, which suggests a stress regime close to permutation between σ_2 and σ_3 axes during this late stage of fold tightening (LSFT, Fig. 19f).

5.2.3. Post Laramide fractures

The last fracture set (P-I) is clearly unrelated to the Laramide contractional event. Calcite twinning consistently recorded post-folding paleostress tensors with a horizontal σ_3 axis oriented E–W, consistent with the opening of late N–S joints, mainly in extensional regime (except in SC66V2). Vein 2 of sample SC82 (Fig. 15) could be interpreted as belonging to this fracture set based on its orientation and its chronological relationship with vein 1, consistently interpreted as belonging to set S-III. These late N–S joints can be tentatively related to the Basin and Range extension mainly described West of Wyoming (Bird, 1998, Fig. 19g).

It should be noticed that the reconstruction of the sequence of fracture development illustrates – although in few cases- the limits of defining of fracture sets based on fracture orientation only (Fig. 15, samples SC58 or SA04 for instance). As a matter of fact, the use of stress tensor chronology obtained independently from calcite twinning analysis can help better constrain the sequence and the range of orientations for each fracture set. In turn, defining accurately the fracture sequence is essential to interpret some ambiguous results of the calcite twin analysis.

5.3. Paleostress evolution at the basin scale

The kinematic scenario of fracture development being well constrained, we propose a rough quantitative reconstruction of the evolution of the state of stress in folded strata of RMA (Fig. 20). As calcite twin data were mainly collected from the Mississippian Madison Fm., we used the only rock mechanics data (Crack Development Curve, CDC) available for Madison samples (Amrouch et al., 2011) despite lithological variations between SMA and RMA (Barbier et al., 2012b–this volume). Thus, because of uncertainties (especially on the CDC), our construction (Fig. 20) cannot be used to reconstruct quantitatively stress magnitudes. However, the trend of evolution of these magnitudes through time remains reliable and clearly suggests stress build-up during each of the three main tectonic events and highlights the common occurrence of stress permutations between strike–slip and compressional stress regimes (Laubach et al., 1992; Yale, 2003).

A comparison between fracture populations at SMA and RMA highlights a more complex fracture population at RMA (7 fracture sets) than at SMA (4 fracture sets, Amrouch et al., 2010a; Bellahsen et al., 2006a) if considering the same Paleozoic formations (Madison and Phosphoria Fms.). Indeed, sets S-I (E–W) and P-I (N–S) were not documented in SMA and set S-II (N–S) is better expressed at RMA than at SMA. Assuming that (1) these sets mark regional tectonic events (see Section 5.2) predating Laramide folding (except for P-I that postdates Laramide) and (2) RMA and SMA have similar overall geometries and kinematic evolution (see Section 5.1), these patterns were probably influenced by the distance to the orogenic fronts (Fig. 19, RMA is located about 120 km East of the present-day Sevier front, SMA at 180 km), despite lithological variations in some Paleozoic formations (Barbier et al., 2012b–this volume) which may affect mechanic properties of rocks (e.g. Laubach et al., 2009).

5.3.1. Pre- and post-Laramide stresses

Concerning the Sevier stress evolution at the basin-scale, the phases of LPS deformation (see Section 5.2) imprinted strata in different way from west to east (Fig. 19a–c): set S-I joints due to a first Sevier stage (E–W shortening in folded structures in Idaho, LPS-1, (Bird, 1998; Craddock, 1992; Craddock and Van der Pluijm, 1999)) formed only in the western part of the Bighorn basin (at RMA). S-III joints correspond to a late Sevier 110°E to 135°E contractional event that affected both sides of the basin, although much extensively to the West (LPS-2). This observation suggests (1) an eastward decrease of tectonic stresses toward the interior of the craton during the Sevier phase (as already suggested by Van der Pluijm et al., 1997), and (2) an eastward propagation of the Sevier orogenic front between the development of S-I and S-III fracture sets in the Sevier foreland.

Accordingly, our results demonstrate that the Sevier-related LPS stress regime evolved from strike–slip (Fig. 20, Sevier LPS 1 and 2) to compressional (Fig. 20, Sevier LPS 3, related to the development of reverse faults (Fig. 14, site 132)) at RMA through time, while such an evolution was not recorded at SMA where the stress regime remained strike–slip during the whole Sevier phase (Amrouch et al., 2011). Thus, the stress regime likely evolved in a different way close (RMA)

and far away (SMA) from the Sevier orogenic front (Fig. 19a–c). This suggests that the evolution of stress regime during stress build-up may consist in a switch from strike–slip to compressional type (Sassi and Faure, 1997), and that, because of SMA was too far from the deformation front, such a switch in stress regime did not occur there.

All these observations establish that, during the Sevier thin-skinned tectonics, a stress build-up likely occurred close to the orogenic front (assuming no change in the cover thickness) in flat-lying strata (i.e. not affected by large-scale deformation). Stresses decreased eastwards, increased through time, and consequently switched from strike–slip to compressional in type close to the orogenic front.

Between these two contractional events, the set S-II (mainly N–S striking veins/joints) developed, the related fractures being more abundant at RMA than at SMA (Fig. 19b). Assuming that this set is related to the foreland flexure in front of the Sevier orogen (see Section 5.2), this observation is consistent with (1) the difference in the mechanical behavior of sedimentary layers in RMA and SMA as demonstrated by Barbier et al. (2012a, 2012b–this volume), and (2) the evolution of the flexure during the Sevier as reconstructed by DeCelles (2004). Indeed, the reconstruction predicts higher extensive stress magnitudes in the western part of the basin, *i.e.* closer to the orogenic front, implying more flexure-related extensional fractures at RMA than SMA.

Finally, the lack of set P-I fractures in the eastern part of the Bighorn basin (SMA) may be also explained by a larger distance to the Basin and Range extensional province, located west of Wyoming (see Bird, 2002; Gries, 1983).

5.3.2. Laramide stresses

In contrast, the Laramide stress evolution was probably similar at RMA and SMA, with the same fracture pattern imprinted in the folded strata during LPS, folding and LSFT stages (Fig. 19d–f). Thus, during the Laramide event, there was presumably no significant difference in terms of stress magnitudes. Indeed, it has been shown that the outermost structure of the basin, the Bighorn Mountains, uplifted early in the Laramide history, during the late Cretaceous (Crowley et al., 2002), supporting the regional distribution of stress.

In order to put some quantitative constraints on the stress evolution at the basin-scale, differential stress magnitudes related to the Laramide event at RMA were compared to those reconstructed at SMA by Amrouch et al. (2010a) (Fig. 21). As only one sample recorded the compressional stress regime related to late stage fold tightening at RMA (Fig. 15, sample SC 58), and in order to be consistent with the approach used at SMA (Amrouch et al., 2010a), we have chosen to compare the evolution of $(\sigma_1-\sigma_h)$ (σ_h being the minimum horizontal principal stress) in the backlimb and the forelimb of the structure for the LPS and LSFT-related strike–slip and compressional stress regimes. To this aim, we reported the values of $(\sigma_1-\sigma_3)$ for the strike–slip regime and we calculate the value of $(\sigma_1-\sigma_2)$ for the compressional regime according to the value of the ratio between differential stresses Φ (see Table 2).

To reliably compare differential stress magnitudes at RMA (Fig. 21a) and SMA (Fig. 21b), which were recorded by calcite twinning at different depths, values obtained at RMA have been corrected and recalculated for a depth similar to the deformation depth at SMA following the equations from Jaeger and Cook (1969) as reported in Lacombe (2007) considering a stress-depth gradient under hydrostatic conditions and a mean friction coefficient of 0.6. A differential burial of about 700 m, estimated from the stratigraphic column of RMA (Durdella, 2001) and SMA (Hennier, 1984), has been used considering the Mississippian Madison Fm. This difference is mainly due to the syn-orogenic Cretaceous formations, which are thicker in the West than in the East due to Sevier flexural subsidence (DeCelles, 2004).

At RMA, two differential stress values were obtained in the backlimb: one from a pre-tilting vein, one from the host–rock matrix. Because the bedding dip is shallow, an uncertainty remains on the pre-tilting or post-tilting timing of the related state of stress. However, we attributed the state of stress obtained in the host–rock to the LSFT event because of the 060°E strike of the maximum principal stress σ_1 (Figs. 14 and 15), which is statistically the strike of post-folding compression. On the contrary, the maximum principal stress σ_1 obtained in the vein strikes 040°E, which is similar to the σ_1 of the Laramide LPS phase (Neely and Erslev, 2009; this study). Note that this interpretation somewhat contradicts a common assumption that calcite twinning in the rock matrix generally reflects LPS rather than late stage fold tightening (Craddock, 1992; Craddock and Van der Pluijm, 1999), but is in agreement with recent findings (Lacombe et al., 2007).

Compared to SMA, a similar $(\sigma_1-\sigma_h)$ evolution is exhibited at RMA (Fig. 21). However, stress perturbation above the basement thrust as identified at SMA (Amrouch et al., 2010a; Bellahsen et al., 2006b) cannot be retrieved at RMA through the reconstruction of stress magnitudes. Moreover, fracture patterns exhibit a clear difference during the Laramide LPS phase: at SMA, LPS-related fractures set was poorly recorded in the forelimb (Barbier et al., 2012b; Bellahsen et al., 2006a), while at RMA, LPS-related fractures of set L-I were observed in both limbs of the fold (Figs. 10 and 11). The lack of LPS-related fracture set has been related to a zone of stress perturbations at the tip of the underlying basement thrust (Bellahsen et al., 2006b) at SMA. This suggests that a similar stress perturbation did not affect the studied sites. This can be explained by the difference of uplift between RMA and SMA and by the subsequent erosion of most of the hinge domain at RMA (Fig. 6): balanced cross sections show that the zone located above the tip of the basement fault splay has been eroded laterally over 4 km. Thus, the lack of evidence of stress perturbation related to the basement fault may simply be due to the lack of outcrops.

The magnitudes of post-folding differential stresses in the backlimb of RMA are higher than the early-folding ones in both limbs (Fig. 21), as in SMA (Amrouch et al., 2010a). This may be related to hardening of the backlimb of RMA, as proposed at SMA (Amrouch et al., 2010a, 2010b): while deformation during the LSFT has been accommodated in the forelimb by late reverse faults (Figs. 4 and 14), reactivation of set S-I fractures (Fig. 14), and propagation of faults within a large basement wedge (Fig. 17), very few structures deformed the backlimb at that stage, allowing an increase of differential stresses.

To sum up, during the Laramide event, differential stresses remained at a sub-constant level of about 20 ± 10 MPa, the formation of widespread LPS-related structures preventing stress increase in the sedimentary layers. Large variations from these values are related either to perturbations at the tip of underlying basement thrusts (as recorded in the forelimb of SMA during LPS) and/or to stress increase where strata remained weakly deformed and did not dissipate stress (as in the backlimb of both folds, during LSFT).

As a result, Laramide differential stress magnitudes were probably not attenuated between RMA and SMA, being likely controlled locally by the structure and kinematics of the individual folds (Fig. 17) rather than by the distance to the orogenic front, in contrast to the eastward attenuation of Sevier stresses. This contrast likely reflects the influence of the structural style, stress magnitudes being mainly controlled by local (basement) structures during thick-skinned tectonics rather than by the distance to the orogenic front as in thin-skinned tectonics settings.

6. Conclusions

In this paper, we carried out structural and microstructural analyses at Rattlesnake Mountain Anticline and compared the results with similar work performed at Sheep Mountain Anticline in order to better constrain the kinematic evolution of Laramide-type thrust-related anticlines, the strain acquisition in folded strata of the Sevier-Laramide foreland, and the stress build-up in the cover.

At the fold scale, structural investigation and construction of displacement profiles point toward a coeval propagation of basement faults underlying the folded cover. These kinematics seem different than in a trishear model as the strain was distributed in the basement although the faults already reached the basement-cover interface.

At the mesoscale, the observed fracture population can be gathered into 7 different sets formed during three main events: the Sevier and Laramide shortening phases and the Basin and Range extension (Fig. 18). At the basin scale, the comparison of structures, fracture patterns and differential stress magnitudes derived from calcite twinning paleopiezometry for each event demonstrates a consistent record of orogenic stresses on both edges of the Bighorn basin during the Laramide thick-skinned tectonics, the level of stress being mainly controlled by the basement-cored, thrust-related individual structures. On the contrary, differences are noticeable in the stress–strain evolution of both sides of the basin during the Sevier orogenic event and the Basin and Range extensional event. Fracture patterns highlight a stress attenuation toward the craton interior, probably related to an increase to the distance to the Sevier orogenic front. During this thin-skinned tectonics phase, this distance to the front also influenced the stress regimes that switch from compressional close to the deformation front (West) to strike–slip in type further away (East). Thus, we likely document an influence of the tectonic style on the stress evolution in space and time at the basin scale.

Beyond regional implications, this study illustrates the potential of combined analyses of macrostructures and micro-mesostructures and paleostress reconstructions to decipher the structural evolution and tectonic history of orogenic forelands.

Acknowledgments

Authors thank Gretchen Hurley and the Bureau of Land Management (BLM) of Cody, Wyoming for their help on the field, Vincent Roche for stimulating discussions and Didier Devaux for providing thin-sections. Authors also thank S. Tavani, F. Storti, E. Erslev and an anonymous reviewer for their criticisms and suggestions, which greatly improved the paper.

References

Ahmadhadi, F., Daniel, J.-M., Azzizadeh, M., Lacombe, O., 2008. Evidence for pre-folding vein development in the Oligo-Miocene Asmari Formation in the Central Zagros Fold Belt, Iran. Tectonics 27, TC1016.

Amrouch, K., Lacombe, O., Bellahsen, N., Daniel, J.-M., Callot, J.-P., 2010a. Stress and strain patterns, kinematics and deformation mechanisms in a basement-cored anticline: Sheep Mountain Anticline, Wyoming. Tectonics 29, TC1005.

Amrouch, K., Robion, P., Callot, J.-P., Lacombe, O., Daniel, J.-M., Bellahsen, N., Faure, J.-L., 2010b. Constraints on deformation mechanisms during folding provided by rock physical properties: a case study at Sheep Mountain anticline (Wyoming, USA). Geophysical Journal International 182 (3), 1105–1123.

Amrouch, K., Beaudoin, N., Lacombe, O., Bellahsen, N., Daniel, J.-M., 2011. Paleostress magnitudes in folded sedimentary rocks. Geophysical Research Letters 38, L17301.

Anastasio, D.J., Fisher, D.M., Messina, T.A., Holl, J.E., 1997. Kinematics of décollement folding in the Lost River Range, Idaho. Journal of Structural Geology 19, 355–368.

Anderson, E.M., 1951. The Dynamics of Faulting, second ed. Oliver and Boyd, Edinburgh. 206 pp.

Angelier, J., 1984. Tectonic analysis of fault slip data sets. Journal of Geophysical Research 89, 5835–5848.

Angelier, J., 1989. From orientation to magnitudes in paleostress determination using fault slip data. Journal of Structural Geology 11, 37–50.

Bai, T., Maerten, L., Gross, M.R., Aydin, A., 2002. Orthogonal cross joints: do they imply a regional stress rotation? Journal of Structural Geology 24, 77–88.

Banerjee, S., Mitra, S., 2004. Remotesurfacemapping using orthophotos and geologic maps draped overdigital elevationmodels: Application to the Sheep Mountain anticline, Wyoming. AAPG Bulletin 88, 1227–1237.

Barbier, M., Hamon, Y., Callot, J.P., Floquet, M., 2012a. Diagenetic influence on fracturation pattern in carbonates: the example of Sheep Mountain (Wyoming, USA). Marine and Petroleum Geology 29, 50–67.

Barbier, M., Leprêtre, R., Daniel, J.-M., Gasparrini, M., Callot, J.-P., Hamon, Y., Lacombe, O., Floquet, M., 2012b. Impact of fracture stratigraphy on the paleo-hydrogeology of the Madison Limestone in two basement-involved folds in the bighorn basin, (Wyoming, USA). Tectonophysics 576–577, 116–132 (this volume).

Beaudoin, N., Bellahsen, N., Lacombe, O., Emmanuel, L., 2011. Fracture-controlled paleohydrogeology in a basement-cored, fault-related fold: Sheep Mountain anticline (Wyoming, USA). Geochemistry, Geophysics, Geosystems 12, Q06011.

Bellahsen, N., Daniel, J.-M., 2005. Fault reactivation control on normal fault growth: an experimental study. Journal of Structural Geology 27, 769–780.

Bellahsen, N., Fiore, P., Pollard, D., 2006a. The role of fractures in the structural interpretation of Sheep Mountain Anticline, Wyoming. Journal of Structural Geology 28, 850–867.

Bellahsen, N., Fiore, P.E., Pollard, D.D., 2006b. From spatial variation of fracture patterns to fold kinematics: A geomechanical approach. Geophysical Research Letters 33, 1–4.

Bellahsen, N., Fournier, M., d'Acremont, E., Leroy, S., Daniel, J.-M., 2006c. Fault reactivation and rift localization: the northeastern Gulf of Aden margin. Tectonics 25. doi:10.1029/2004TC001626.

Bergbauer, S., Pollard, D.D., 2004. A new conceptual fold–fracture model including prefolding joints, based on field data from the Emigrant Gap anticline, Wyoming. GSA Bulletin 116, 294–307.

Billi, A., Salvini, F., 2003. Development of systematic joints in response to flexure-related fibre stress in flexed foreland plates: the Apulian forebulge case history, Italy. Journal of Geodynamics 36, 523–536.

Bird, P., 1998. Kinematic history of the Laramide orogeny in latitudes 35°-49°N, western United States. Tectonics 17, 780–801.

Bird, P., 2002. Stress direction history of the western United States and Mexico since 85 Ma. Tectonics 21, TC001319.

Blackstone Jr., D.L., 1986. Structural geology—North-west margin, Bighorn Basin: Park County, Wyoming, and Carbon County, Montana. In: Garrison, P.B. (Ed.), Geology of the Beartooth uplift and adjacent basins: Montana Geological Society and Yellowstone – Bighorn Research Association Joint Field Conference and Symposium, pp. 125–136.

Boiron, M.-C., Cathelineau, M., Banks, D.A., Fourcade, S., Vallance, J., 2003. Mixing of metamorphic and surficial fluids during the uplift of the Hercynian upper crust: consequences for gold deposition. Chemical Geology 194, 119–141.

Brown, W.G., 1988. Deformational style of Laramide uplifts in the Wyoming foreland. In: Schmidt, C.J., Perry Jr., W.J. (Eds.), Interaction of the Rocky Mountain Foreland and the Cordilleran Thrust Belt: G.S.A. Memoir, 171, pp. 1–26. Boulder.

Brown, W.G., 1993. Structural style of Laramide basement-cored uplifts and associated folds. In: Snoke, A.W., Steidtmann, J.R., Roberts, S.M. (Eds.), Geology of Wyoming: Geological survey of Wyoming Memoir, No. 5, pp. 312–371.

Bump, A.P., 2003. Reactivation, tri-shear modeling, and folded basement in Laramide uplifts: implications for the origins of intra-continental faults. GSA Today 4–10.

Callot, J.-P., Robion, P., Sassi, W., Guiton, M.L.E., Faure, J.-L., Daniel, J.-M., Mengus, J.-M., Schmitz, M., 2010. Magnetic characterisation of folded aeolian sandstones: Interpretation of magnetic fabrics in diamagnetic rocks. Tectonophysics 495, 230–245.

Cartwright, J.A., Trudgill, B.D., Mansfield, C.S., 1995. Fault growth by segment linkage: an explanation for scatter in maximum displacement and trace length data from Canyonlands grabens of SE Utah. Journal of Structural Geology 17, 1319–1326.

Cathelineau, M., Fourcade, S., Clauer, N., Buschaert, S., Rousset, D., Boiron, M.-C., Meunier, A., Lavastre, V., Javoy, M., 2004. Dating multistage paleofluid percolations: A K-Ar and 18O/16O study of fracture illites from altered Hercynian plutonites at the basement/cover interface (Poitou High, France). Geochimica et Cosmochimica Acta 68, 2529–2542.

Cooke, M.L., 1997. Fracture localization along faults with spatially varying friction. Journal of Geophysical Research 102, 22,425–22,434.

Couzens, B.A., Dunne, W.M., 1994. Displacement transfer at thrust terminations: Saltville thrust and Sinking Creek anticline, Virginia, U.S.A. Journal of Structural Geology 16, 781–793.

Craddock, J.P., 1992. Transpression during tectonic evolution of the Idaho-Wyoming fold-and-thrust belt. Geological Society of America Memoir 179, 125–139.

Craddock, J., Van der Pluijm, B.A., 1999. Sevier–Laramide deformation of the continental interior from calcite twinning analysis, west-central North America. Tectonophysics 305, 275–286.

Crowley, P.D., Reiners, P.W., Reuter, J.M., Kaye, G.D., 2002. Laramide exhumation of the Bighorn Mountains, Wyoming: An apatite (U-Th)/He thermochronology study. Geology 30, 27–30.

DeCelles, P.G., 1994. Late Cretaceous-Paleocene synorogenic sedimentation and kinematic history of the Sevier thrust belt, northeast Utah and Southwest Wyoming. Bulletin of the Geological Society of America 106, 36–56.

DeCelles, P.G., 2004. Late Jurassic to Eocene evolution of the Cordilleran Thrust Belt and foreland basin system, Western U.S.A. American Journal of Science 304, 105–168.

DeCelles, P.G., Gray, M.B., Ridgway, K.D., Cole, R.B., Srivastava, P., Pequera, N., Pivnik, D.A., 1991. Kinematic history of a foreland uplift from Paleocene synorogenic conglomerate, Beartooth Range, Wyoming and Montana. GSA Bulletin 103, 1458–1475.

DeCelles, P.G., Gehrels, G.E., Quade, J., Ojha, T.P., 1998. Eocene-early Miocene foreland basin development and the history of Himalayan thrusting, western and central Nepal. Tectonics 17, 741–765.

Durdella, M.J., 2001. Mechanical Modeling of Fault-related Folds: West Flank of the Bighorn Basin, Wyoming. M.S. Thesis, Purdue University.

Engelder, T., 1987. Joints and some fractures in rocks. In: Atkinson, B. (Ed.), Fracture Mechanics of Rock. Academic Press, pp. 27–69.

Erslev, E.A., 1986. Basement balancing of Rocky Mountain foreland uplifts. Geology 14, 259–262.

Erslev, E.A., 1991. Trishear fault-propagation folding. Geology 19, 617–620.

Erslev, E.A., 1995. Heterogeneous Laramide deformation in the Rattlesnake Mountain Anticline, Cody, Wyoming. Field Trip 7, 141–150.

Erslev, E.A., Koenig, N.V., 2009. Three-dimensional kinematics of Laramide, basement-involved Rocky Mountain deformation, USA: Insights from minor faults and GIS-enhanced structure maps. GSA Memoirs 204, 125–150.

Erslev, E.A., Mayborn, K.R., 1997. Multiple geometries and modes of fault propagation folding in the Canadian thrust belt. Journal of Structural Geology 19, 321–335.
Erslev, E.A., Rogers, J.L., 1993. Basement-cover geometry of Laramide fault- propagation folds. In: Schmidt, C.J., Chase, R., Erslev, E.A. (Eds.), Laramide basement deformation in the Rocky Mountain foreland of the western United States: G.S.A. Special Paper, 280, pp. 125–146.
Essarraj, S., Boiron, M.-C., Cathelineau, M., Banks, D.A., Benharref, M., 2005. Penetration of surface-evaporated brines into the Proterozoic basement and deposition of Co and Ag at Bou Azzer (Morocco): Evidence from fluid inclusions. Journal of African Earth Sciences 41, 25–39.
Etchecopar, A., 1984. Etude des états de contraintes en tectonique cassante et simulation de déformations plastiques [Ph.D thesis]: Montpellier, France, Université Montpellier, 270 pp.
Ferrill, D.A., Morris, A.P., Evans, M.A., Burkhard, M., Groshong Jr., R.H., Onasch, C.M., 2004. Calcite twin morphology: a low-temperature deformation geothermometer. Journal of Structural Geology 26, 1521–1529.
Fiore Allwardt, P., Bellahsen, N., Pollard, D.D., 2007. Curvature and fraturing based on global positioning system data collected at Sheep Mountain anticline, Wyoming. Geosphere 3, 408–421.
Fischer, M.P., Wilkerson, M.S., 2000. Predicting the orientation of joints from fold shape: Results of pseudo–three-dimensional modeling and curvature analysis. Geology 28, 15–18.
Fischer, M.P., Woodward, N.B., Mitchell, M.M., 1992. The kinematics of break-thrust folds. Journal of Structural Geology 19, 321–335.
Ford, M., Williams, E.A., Artoni, A., Vergés, J., Hardy, S., 1997. Progressive evolution of a fault-related fold pair from growth strata geometries, Sant Llorenç de Morunys, SE Pyrenees. Journal of Structural Geology 19, 413–441.
Fourcade, S., Michelot, J.L., Buschaert, S., Cathelineau, M., Freiberger, R., Coulibaly, Y., Aranyossy, J.F., 2002. Fluid transfers at the basement/cover interface: Part I. Subsurface recycling of trace carbonate from granitoid basement rocks (France). Chemical Geology 192, 99–119.
Gries, R., 1983. North–south compression of Rocky Mountain foreland structures. In: Lowell, J.D. (Ed.), Rocky Mountain Foreland Basin and Uplifts. Rocky Mt. Assoc. of Geol., Denver, Colorado, pp. 9–32.
Guiton, M., Sassi, W., Leroy, Y., Gauthier, B., 2003. Mechanical constraints on the chronology of fracture activation in the folded Devonian sandstone of the western Moroccan Anti-Atlas. Journal of Structural Geology 25, 1317–1330.
Hancock, P.L., 1985. Brittle microtectonics; principles and practice. Journal of Structural Geology 7, 437–457.
Harris, J.H., Van der Pluijm, B.A., 1998. Relative timing of calcite twinning strain and fold-thrust belt development; Hudson Valley fold-thrust belt, New York, USA. Journal of Structural Geology 20, 21–31.
Hennier, J.H., 1984. Structural analysis of the Sheep Mountain Anticline, Bighorn basin, Wyoming. A&S University, Texas. 118 pp.
Jaeger, J.C., Cook, N.G.W., 1969. Fundamentals of Rock Mechanics. Chapman and Hall, New York.
Johnson, K., Johnson, A.M., 2002. Mechanical models of trishear-like folds. Journal of Structural Geology 24, 277–287.
Jordan, T.E., 1981. Thrust loads and foreland basin evolution, Cretaceous, western United States. AAPG Bulletin 65, 2506–2520.
Katz, D.A., Eberli, G.P., Swart, P.K., Smith, L.B., 2006. Tectonic-hydrothermal brecciation associated with calcite precipitation and permeability destruction in Mississippian carbonate reservoirs, Montana and Wyoming. AAPG Bulletin 90, 1803–1841.
Kim, Y.-S., Sanderson, D.J., 2005. The relationship between displacement and length of faults: a review. Earth-Science Reviews 68, 317–334.
Lacombe, O., 2001. Paleostress magnitudes associated with development of mountain belts: Insights from tectonic analyses of calcite twins in the Taiwan Foothills. Tectonics 20, 834–849.
Lacombe, O., 2007. Comparison of paleostress magnitude from calcite twins with contemporary stress magnitudes and frictional sliding criteria in the continental crust: Mechanical implications. Journal of Structural Geology 29, 86–99.
Lacombe, O., 2010. Calcite twins, a tool for tectonic studies in thrust belts and stable orogenic forelands. Oil and Gas Science and Technology 65, 809–838.
Lacombe, O., 2012. Do fault slip data inversions actually yield 'paleostresses' that can be compared with contemporary stresses? A critical discussion. C.R. Geoscience 334 (3), 159–173.
Lacombe, O., Laurent, P., 1992. Determination of principal stress magnitudes using calcite twins and rock mechanics data. Tectonophysics 202, 83–93.
Lacombe, O., Angelier, J., Laurent, Ph., Bergerat, F., Tourneret, Ch., 1990. Joint analyses of calcite twins and fault slips as a key for deciphering polyphase tectonics: Burgundy as a case study. Tectonophysics 182, 279–300.
Lacombe, O., Angelier, J., Laurent, P., 1993. Calcite twins as markers of recent compressional events in an active orogen : the reefal limestones of southern Taiwan as a case-study. Comptes Rendus de l' Academie des Sciences Serie II 316 (12), 1805–1813.
Lacombe, O., Amrouch, K., Mouthereau, F., Dissez, L., 2007. Calcite twinning constraints on late Neogene stress patterns and deformation mechanisms in the active Zagros collision belt. Geology 35 (3), 263–266. doi:10.1130/G23173A.1.
Lacombe, O., Bellahsen, N., Mouthereau, F., 2011. Fracture patterns in the Zagros Simply Folded Belt (Fars): New constraints on early collisional tectonic history and role of basement faults. In: Lacombe, O., Grasemann, B., Simpson, G. (Eds.), Geodynamic evolution of the Zagros: Geological Magazine, 148, pp. 940–963.
Lamarche, G., Proust, J.N., Nodder, S.D., 2005. Long-term slip rates and fault interactions under low contractional strain, Wanganui Basin, New Zealand. Tectonics 24, TC4004.
Lash, G.G., Engelder, T., 2007. Jointing within the outer arc of a forebulge at the onset of the Alleghanian Orogeny. Journal of Structural Geology 29, 774–786.
Laubach, S.E., Tyler, R., Ambrose, W.A., Tremain, C.M., Grout, M.A., 1992. Preliminary map of fracture patterns in coal in the western United States. Wyoming Geological Association 43, 253–267.
Laubach, S.E., Olson, J., Gross, M.R., 2009. Mechanical and fracture stratigraphy. AAPG Bulletin 93, 1413–1427.
Laurent, P., Kem, H., Lacombe, O., 2000. Determination of deviatoric stress tensors based on inversion of calcite twin data from experimentally deformed monophase samples. Part II. Axial and triaxial stress experiments. Tectonophysics 327, 131–148.
Lin, A.T., Watts, A.B., 2002. Origin of the West Taiwan basin by orogenic loading and flexure of a rifted continental margin. Journal of Geophysical Research 107, JB000669.
Lovely, P., Zahasky, C., Pollard, D.D., 2010. Fold geometry at Sheep Mountain anticline, Wyoming, constructed usingairbone laser swath mapping data, outcrop-scale geologic mapping, and numerical interpolation. Journal of Geophysical Research 115, B12414.
Marshak, S., Karlstrom, K., Timmons, J.M., 2000. Inversion of Proterozoic extensional faults: An explanation for the pattern of Laramide and Ancestral Rockies intracratonic deformation, United States. Geology 28, 735–738.
McQuarrie, N., DeCelles, P., 2001. Geometry and structural evolution of the central Andean backthrust belt, Bolivia. Tectonics 20, 669–692.
McQuillan, H., 1974. Fracture patterns on Kuh-e Asmari Anticline, Southwest Iran. AAPG Bulletin 58, 236–246.
Mercadier, J., Richard, A., Boiron, M.-C., Cathelineau, M., Cuney, M., 2010. Migration of brines in the basement rocks of the Athabasca Basin through microfracture networks (P-Patch U deposit, Canada). Lithos 115, 121–136.
Mouthereau, F., Tensi, J., Bellahsen, N., Lacombe, O., De Boisgrollier, T., Kargar, S., 2007. Tertiary sequence of deformation in a thin-skinned/thick-skinned collision belt: The Zagros Folded Belt (Fars, Iran). Tectonics 26, TC5006.
Narr, W., Suppe, J., 1994. Kinematics of basement-involved compressive structures. American Journal of Science 294, 802–860.
Neely, T.G., Erslev, E.A., 2009. The interplay of fold mechanisms and basement weaknesses at the transition between Laramide basement-involved arches, north-central Wyoming, USA. Journal of Structural Geology 31, 1012–1027.
Peacock, D.C.P., Sanderson, D.J., 1991. Displacements, segment linkage and relay ramps in normal fault zones. Journal of Structural Geology 13, 721–733.
Pierce, W.G., 1966. Geologic map of the Cody quadrangle, Park County, Wyoming. U.S. Geological Survey Geologic Quadrangle Map GQ-542, Scale 1:62,500.
Pierce, W.G., Nelson, W.H., 1968. Geologic map of the Pat O'Hara Mountain Quadrangle, Park County, Wyoming. U.S. Geological Survey Geologic Quadrangle Map GQ-0755, Scale 1:62,500.
Pranter, M.J., Reza, Z.A., Budd, D.A., 2006. Reservoir-scale characterization and multiphase fluid-flow modelling of lateral petrophysical heterogeneity within dolomite facies of the Madison Formation, Sheep Canyon and Lysite Mountain, Wyoming, USA. Petroleum Geosciences 12, 29–40.
Quintà, A., Tavani, S., 2012. The foreland deformation in the south-western Basque-Cantabrian Belt (Spain). Tectonophysics. 576–577, 14–19 (this issue).
Rives, T., Rawsley, K.D., Petit, J.-P., 1994. Analogue simulation of natural orthogonal joint set formation in brittle varnish. Journal of Structural Geology 16, 419–429.
Rocher, M., Lacombe, O., Angelier, J., Chen, H.-W., 1996. Mechanical twin sets in calcite as markers of recent collisional events in a fold-and-thrust belt: Evidence from the regal limestones of southwestern Taiwan. Tectonics 15, 984–996.
Rocher, M., Baize, S., Angelier, J., Lozac'h, Y., Lemeille, F., Cushing, M., 2004. Intraplate paleostresses reconstructed with calcite twinning and faulting: improved method and application to the Lorraine platform area (eastern France). Tectonophysics 387, 1–21.
Roger, C.M., Myers, D.A., Engelder, T., 2004. Kinematic implications of joint zones and isolated joints in the Navajo Sandstone at Zion National Park, Utah: Evidence for Cordilleran relaxation. Tectonics 23, TC1007.
Rowe, K.J., Rutter, E.H., 1990. Paleostress estimation using calcite twinning: experimental calibration and application to nature. Journal of Structural Geology 12, 1–17.
Sanderson, D.J., 1982. Models of strain variation in nappes and thrust sheets: A review. Tectonophysics 88, 201–233.
Sassi, W., Faure, J.-L., 1997. Role of fault and layer interfaces on the spatial variation of stress regimes in basins: inferences from numerical modeling. Tectonophysics 266, 101–109.
Savage, H.M., Shackelton, J.R., Cooke, M.L., Riedel, J.J., 2010. Insights into fold growth using fold-related joint patterns and mechanical stratigraphy. Journal of Structural Geology 32, 1466–1475.
Shackelton, J.R., Cooke, M.L., 2007. Is plane strain a valid assumption in non-cylindrical fault-cored folds? Journal of Structural Geology 29, 1229–1240.
Srivastava, D., Engelder, T., 1990. Crack-propagation sequence and pore-fluid conditions during fault-bend folding in the Appalachian Valley and Ridge, Central Pennsylvania. GSA 102, 116–128.
Stanton, H.I., Erslev, E.A., 2004. Sheep Mountain Anticline: backlimb tightening and sequential deformation in the Bighorn Basin, Wyoming. Wyoming Geological Association Guidebook 53, 75–87.
Stearns, D.W., 1978. Faulting and forced folding in the Rocky Montains foreland. In: Matthews, V. (Ed.), Laramide folding associated with basement block faulting in the western United States: Geological Soc. of America, Memoir, 151, pp. 1–37.
Stearns, D.W., Friedman, M., 1972. Reservoirs in fractured rock. AAPG Memoir 16, 82–106.
Stone, D.S., 1993. Basement-involved thrust-generated folds as seismically imaged in the subsurface of the central Rocky Mountain foreland. In: Schmidt, C.J., Chase, R.B., Erslev, E.A. (Eds.), Laramide basement deformation in the Rocky Mountain of the western United States: Geological Society of America Special Paper, 280, pp. 271–318. Boulder.
Storti, F., Salvani, F., 2001. Fault re-activation, fracture patterns, and cataclasite development in the carbonate rocks of the Narni Anticline. The evolution of a model trap structure in the Apennines, Italy. Journal of Petroleum Geology 24, 171–190.
Tavani, S., Storti, F., Fernández, O., Muñoz, J.A., Salvini, F., 2006. 3-D deformation pattern analysis and evolution of the Añisclo anticline, southern Pyrenees. Journal of Structural Geology 28, 257–275.

Tavani, S., Mencos, J., Bausà, J., Muñoz, J.A., 2011. The fracture pattern of the Sant Corneli Bóixols oblique inversion anticline (Spanish Pyrenees). Journal of Structural Geology 33, 1662–1680.
Thorbjornsen, K.L., Dunne, W.M., 1997. Origin of a thrust-related fold: geometric vs kinematic tests. Journal of Structural Geology 19, 303–319.
Van der Pluijm, B.A., Craddock, J.P., Graham, B.R., Harris, J.H., 1997. Paleostress in cratonic North America: implications for deformation of continental interiors. Science 277, 794–796.
Varga, R.J., 1993. Rocky Mountain foreland uplifts: Products of rotating stress field or strain partitioning? Geology 21, 1115–1118.
Walsh, J.J., Nicol, A., Childs, C., 2002. An alternative model for the growth of faults. Journal of Structural Geology 27, 1669–1675.
Yale, D.P., 2003. Fault and stress magnitude controls on variations in the orientation of *in situ* stress. In: Ameen, M. (Ed.), Fracture and in-situ stress characterization of hydrocarbons reservoirs: Geological Society, London, Special Publication, 203, pp. 55–64.